The University of Oklahoma

Graduate College

Toward Measuring a Charge-Parity Violating Electric Dipole Moment of the Electron: Production and Pseudo-Continuous Resonance Enhanced Multiphoton Ionization of $^{208}Pb^{19}F$

A Dissertation

Submitted to the Graduate Faculty

in partial fulfillment of the requirements for the

Degree of

Doctor of Philosophy

By

Poopalasingam Sivakumar
Norman, Oklahoma
2009

Toward Measuring a Charge-Parity Violating Electric Dipole Moment of the Electron: Production and Pseudo-Continuous Resonance Enhanced Multiphoton Ionization of $^{208}Pb^{19}F$

A Dissertation Approved for the
Homer L. Dodge Department of Physics and Astronomy

By

Neil Shafer-Ray (Chair)

Deborah K. Watson

Eric Abraham

Greg Parker

John E. Furneaux

Roger Frech(Department of Chemistry)

எனது அன்புக்குரிய பெற்றோர்

திரு. பொன்னையா பூபாலசிங்கம், திருமதி. மனோன்மனி பூபாலசிங்கம்

அவர்களுக்கு இந்த ஆய்வுக் கட்டுரையை சமர்பிக்கிறேன்.

I dedicate this thesis to my loving parents
Poopalasingam Ponniah and Manonmany Poopalasingam

Acknowledgements

My long journey to a Ph.D could not have happened without the encouragement and guidance of many people. I would like to express my gratitude to all these people, including those mentioned and not mentioned here.

Of course, this journey did not begin at the University of Oklahoma. I would like to thank my siblings Gopi, Moorthy, Sankar, Gomathy, Pooma, Selvam, and their children for their love and support. My thanks also go out to my cousins for their encouragement. My very special thanks to my parents Poopalasingam Ponniah and Manonmany Poopalasingam whom I owe everything I am today. Their unwavering faith and confidence in my abilities was critical from the first day at Idaikkadu Maha Vidyalayam until my last day at the University of Oklahoma.

I would like to thank my advisor professor Neil Shafer-Ray for his supervision, support, and guidance from the early stage of my research as well as giving me extraordinary experience throughout my Ph.D. education. In addition, he was always accessible and willing to help me in my research and writing on this thesis. I could not imagine having a better advisor for my thesis dissertation.

I would also like to express my deep gratitude to Professor George Kalbfleisch who worked side by side with myself and Professor Shafer-Ray until his untimely death during my third year as a graduate student. His motivation and encouragement to learning physics gave me the confidence to begin my graduate work.

I gratefully acknowledge my laboratory partner throughout this endeavor, graduate student Chris McRaven. His involvement, experience, and laboratory skills kept the experiment moving forward. He also introduced me to the music that kept us moving forward all of

those late nights.

Many thanks go to the new crop of graduate students, Milinda Rupasinghe and Tao Yang, for their advice and critical comments about the experiment and for their untiring proof-reading of multiple versions of this thesis dissertation. The experiment has been left in good hands! I also thank Parshuram Dahal who kept us fresh in the office.

Many thanks to all my friends and classmates who studied, relaxed, and traveled with me. Also thanks to those of them who read this dissertation and provided useful input. Others that should be mentioned here include Dr Trevor J Sears and Professor Gregory E. Hall of Brookhaven National Laboratory for their encouragement and help in the analysis of hyperfine constants. My sincere thanks also goes to the staff from computer resources (Andy Feld), electronic facilities (Adrienne Wadeinstrument), instrument shop (Joel Young, Barry Bergeron, Bob Littell(passed away), and Sean Atteberry), and front office (Danette Loyd, Debbie Barnhill, Sharon Widner, and Mary Morrison). I wish to express my warm and sincere thanks to my advisory committee members Professor Deborah K. Watson, Professor Eric Abraham, Professor Greg Parker, Professor John E. Furneaux, and Professor Roger Frech (Department of Chemistry).

Also thanks to Professors Shafer-Ray, Watson, and Parker for helping to land my first job. I will think of them when starting the next leg of my journey.

Contents

List of Figures

List of Tables

Abstract

Over one half century has passed since the possible violation of time reversal symmetry was proposed by Purcell and Ramsey. The Standard Model predicts that a value of the e-EDM $|d_{e,SM}| < 10^{-38} e \cdot \text{cm}$ that is beyond the reach of current experiment. At the same time, theories beyond the Standard Model predict an e-EDM at or near the current experimental level of $|d_{e,exp}| < 1.3 \times 10^{-27} e \cdot \text{cm}$. Thus an e-EDM is a great place look for physics beyond the Standard Model.

The existence of a permanent electric dipole moment would break the usual degeneracy between states of a molecule that only differ by the sign of the projection of their total angular momentum onto the axis of an external electric field. Heavy polar diatomic molecules are expected to be particularly sensitive to an e-EDM. Among the many proposed e-EDM molecules, the PbF molecule may be uniquely sensitive to an e-EDM because the magnetic moment of its ground state vanishes at a magic value of external electric field (67 kV/cm).

This thesis reports on the creation of a stable molecular beam source of PbF based on the serendipitous discovery of the reaction of lead vapor and MgF_2 . This thesis also gives the result of the following achievements enabled by this source: (1) The first demonstration of resonant enhanced multiphoton ionization(REMPI) detection of the molecule. (2) Experimental measurement and analysis of the rotational spectra of the 0-0 band of

the B$\leftarrow$ X_1 transition of PbF. This measurement determines the rotational temperature of our source. (3) Measurement of appearance ionization from the B and D states of the PbF molecule. This measurement improves the known ionization potential of PbF from 7.5 ± 0.3 eV to 7.54 ± 0.01 eV, (4) Achievement of a multiphoton ionization probe of PbF that is doubly resonant with the A$\leftarrow$ X_1 and D $\leftarrow$ A transitions. This scheme allows for fully state resolved spectra of the molecule. (5) Direct measurement of the lifetime of the PbF molecule. (6) Measurement of hyperfine constants that model the interaction of the unpaired electron in $^{208}Pb^{19}F$ with the ^{19}F nucleus.

In addition to these achievements, a new type of ultra-sensitive REMPI is reported. Whereas conventional REMPI is typically carried out with pulsed laser systems, this new technique, dubbed pc-REMPI, occurs with a combination of continuous and pseudo-continuous lasers. This technique improves the detection sensitivity of the original PbF REMPI probe by a factor of 100. At the same time, the technique improves the spectra linewidth from 2 GHz to 90 MHz, allowing for full resolution of the hyperfine structure of the molecule.

Chapter 1

Introduction

In this thesis I describe progress toward measurement of a charge-parity violating electric dipole moment of the electron using the PbF molecule. This chapter begins with a description of time reversal invariance and electric dipole moments (section 1.1.) Section 1.2 gives an overview of what is known about the electric dipole moment of the electron (e-EDM). Section 1.3 describes how atoms and molecules may be used to search for an e-EDM. Section 1.4 describes additional features of PbF molecules that make it particularly suited to a search for the e-EDM.

1.1 Time reversal invariance and electric dipole moments

Until the early 1950s, it was widely believed that fundamental interactions of nature should be invariant in space inversion (parity, P), interchange of particles and anti-particles (charge conjugation, C), and time reversal (T). The possible violation of time reversal symmetry was proposed by Purcell and Ramsey in 1950 [16]. In 1956, T. D. Lee and C. N. Yang proposed that parity conservation might be violated in the weak interaction after analysis of particle decay experiments at Brookhaven's Cosmotron particle accelerator [69].

This hypothesis was confirmed by C. S. Wu and collaborators in 1956 who found a clear violation of parity symmetries in the β emission of polarized cobalt-60 (^{60}Co) [9]. Soon after the first observation of parity violation, CP symmetry was proposed by Lev Landau in 1957 as a true symmetry between matter and anti-matter [42].

In 1951, Julian Schwinger proved the CPT theorem which states CPT symmetry is required

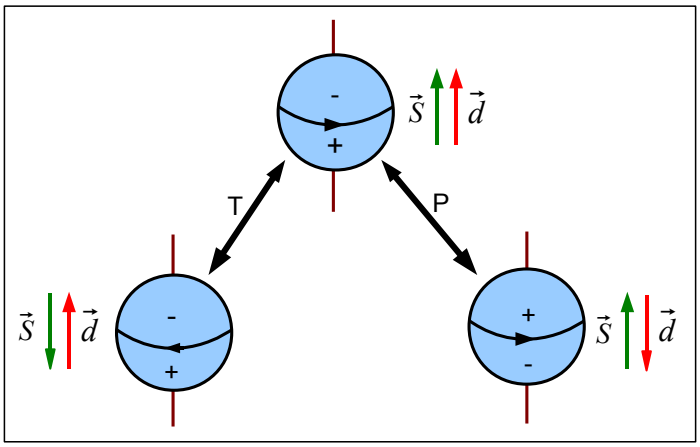

Figure 1.1: For particle obeying Fermi spin statistics, an electric dipole moment (EDM) must be proportional to spin. As a result, such an EDM would break both T and P symmetries.

for Lorentz invariance. If one accepts the CPT theorem, then a system that violates CP symmetry must also violate T symmetry. Today the CPT theorem is so widely accepted that the terms *T violation* and *CP violation* are often used interchangeably. As we shall see, an electric dipole moment proportional to the spin of a particle is CP violating. It is, however, not the only mechanism for CP violation. In fact, while no electric dipole moment

of this type has been observed, CP violation was first observed by Fitch and Cronin in the decay of the long-lived natural K-Meson [30], thereby disproving the 1957 hypothesis of Landau.

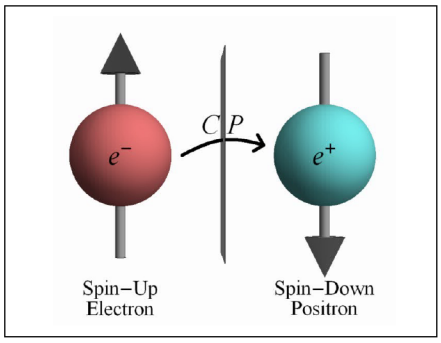

Figure 1.2: The CP operator reverse the spatial axis and switch the particles to antiparticles.

1.2 The electric dipole moment of the electron and CP violation

It is easy to imagine that the charge density of an electron is not uniformly distributed, resulting in an electric dipole moment. However, consideration of the periodic table of the elements greatly constrains the possible nature of such a non-uniform charge distribution. Because the periodic table is built from orbitals that fill in pairs, each electron must have two and only two spin degrees of freedom. A second quantum degree of freedom giving the direction and or magnitude of an electric dipole moment would alter this Fermi statistics. Thus, if the electron is to have an electric dipole moment, it must be proportional to the electron spin. Any other option will alter chemistry as we know it.

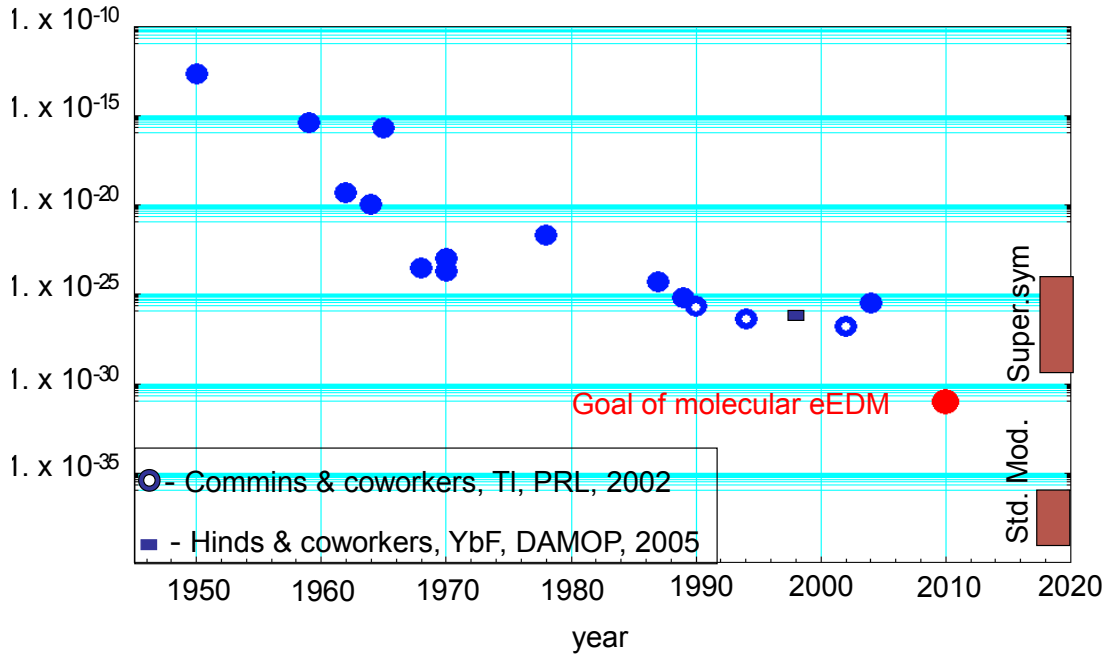

Figure 1.3: Electric dipole moment of the electron measurements in the literature and the new limit may be achieved by using heavy polar molecules. Black bars show the significance of the Standard Model[18] and Supersymmetry [60]

An electric dipole moment simply proportional to spin is inherently T and P violating. To see this, consider Figure 1.1. If time is reversed, spin reverses but the charge distribution of the electron does not. Similarly, if parity is reversed, spin does not reverse but the charge distribution does. Thus a measurement of the electron's electric dipole moment could be used to determine both the direction of time and the fundamental handedness of the Universe. As such, the existence of an EDM proportional to spin is both T and P violating.

The Standard Model predicts that a value of the e-EDM $|d_{e,SM}| < 10^{-38} e \cdot \text{cm}$ that is beyond the reach of current experiment [19]. At the same time, theories beyond the

standard model predicts an e-EDM at or near the current experimental level of $|d_{e,exp}| < 1.3 \times 10^{-27} e{\cdot}\text{cm}$ [60]. Thus an e-EDM is a great place to look for physics beyond the Standard Model.

1.3 e-EDM in atoms and molecules

Purcell and Ramsey [16] first proposed to search for an electric dipole moment by probing the energy level structure of a neutral atom in a strong electric field. This technique looks for a lifting of the usual degeneracy between the states of an atom or molecule in a pure electric field that differ only in the sign of the projection M of total angular momentum on the electric field axis.

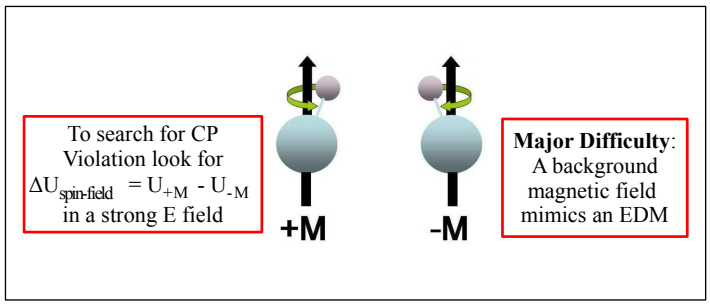

Figure 1.4: A nonzero permanent electric dipole moment would cause a lifting in the degeneracy of $\pm M_F$ states.

Schiff pointed out that the average acceleration, and hence average electric field, of any non-relativistic electron in a stationary atom must be zero. As a result, an atom consisting of nonrelativistic electrons can not exhibit a first-order perturbation due to an electric dipole moment [41]. In this same publication, Schiff points out that the average electric field seen

by an electron with relativistic orbital speeds can be very large. Larger, in fact, than the laboratory field applied to polarize the atom.

In 1967 Sandars quantified the effect of a P and T violating electric dipole moment on the energy levels of an atom. Specifically Sandars found that paramagnetic atoms exhibit an enhancement factor $R = d_{atom}/d_e$ that is roughly proportional to $\alpha^2 Z^3 \alpha_D$ where α is the fine structure constant, Z is the nuclear charge, and α_D is the atomic polarizability of the atom [56, 52].

At the time of the writing of this thesis, the current limit on the electric dipole moment of the electron is found from measurement of the energy difference between the $M = 1$ and $M = -1$ states of the $^2\Pi_{1/2}(F = 1)$ state of Tl atoms in a magnetic field that is alternatively parallel to and anti-parallel to a strong electric field. Electronic structure calculations indicate that this energy difference is given by $585 \times d_e E_{lab}$ where d_e is the electric dipole moment of the electron and $R = -585$ is the calculated enhancement factor [72]. The Commins experiment determines a limit on the e-EDM after confirming that the energy splitting agrees for the parallel and anti-parallel case to a precision of 20 μHz [17] .

1.4 The PbF molecular e-EDM experiment

As early as 1967, Sandars suggested heavy polar molecules as an attractive candidate for a measurement of d_e [53]. Heavy polar diatomic molecules are more sensitive to an electric dipole moment of the electron because molecules have states of opposite electronic parity separated by very little energy. Because of this, a very weak electric field can create strongly polarized states for which the average electronic field seen by an unpaired electron is comparable to the internal field of the molecule [55]. Careful calculations show that heavy

paramagnetic molecules are $1,000$ to $10,000$ times more sensitive to an e-EDM than are molecules [39].

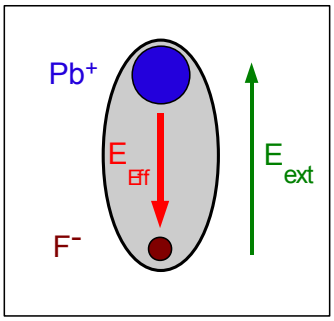

Figure 1.5: Heavy polar molecules are a promising candidate for e-EDM experiments due to an exaggerated polarizability that gives access to a large internal electric field - dipole moment interaction.

Two molecular e-EDM experiments with comparable sensitivity to the Tl experiment have been carried out. One involves a probe of metastable PbO molecules [12] and the other YbF molecules [27]. Although different in detail, both of these experiments are similar to the Tl experiment in that they search for an e-EDM by looking for the difference in the energy splitting between an $F = 1, M = 1$ and $F = 1, M = -1$ state of the system for the case of a electric field parallel to and anti-parallel to a magnetic field. These experiments are extremely challenging for several reasons. One is that a small change in the magnitude of the magnetic field upon reversal of the field directions can lead to an effect orders of magnitude larger than that of a possible e-EDM. A second challenge that is particularly severe for molecules is that the magnetic moment depends strongly on the magnitude of the electric field. Thus the magnitude of both the electric and magnetic fields must be precisely

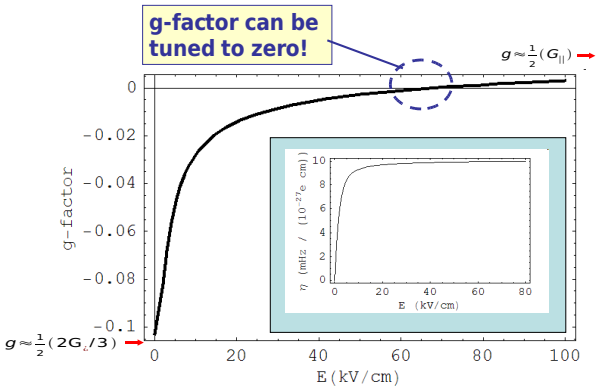

Figure 1.6: PbF molecule has additional features that at a critical value of external electric field, its g-factor vanishes [50]

controlled during field reversals.

The PbF molecule has an additional advantage over other molecular e-EDM experiments. Because it is a $^2\Pi_{1/2}$ molecule, its magnetic g-factor is small. More importantly, the g factor vanishes at a magic value of external electric field (67 kV/cm) [50]. This allows for a magnetic balance measurement of the electric dipole moment: Here one measures the electric field magnitude for which the polarization of a beam of PbF molecules is unaffected by an applied magnetic field. If this magnitude is found to be different for the case of an electric field parallel a to magnetic field and the case of an electric field anti-parallel to a magnet field, one would have evidence for an electric dipole moment. By searching for the value of electric field for which the magnetic moment vanishes, one greatly reduces the sensitivity of the experiment to the precise value of the magnetic field.

The work of this thesis is not the design of such a magnetic balance e-EDM experiment. Rather it is in the development of production and detection techniques necessary to take

advantage of the promising properties of the PbF molecule as a probe of the e-EDM. In chapter 2, the production of a beam source of PbF is described. Chapter 3 describes the direct measurement of the lifetime of the D state of PbF. Knowledge of this lifetime was critical to the development of a new molecular detection scheme ideally suited to a molecular e-EDM measurement. Chapter 4 describes this technique (which we have named pc-REMPI) in detail and the application of pc-REMPI to the measurement of the hyperfine constants of the X_1 and A states of the $^{208}Pb^{19}F$ molecule. Chapter 5 gives results and conclusions.

Chapter 2

Production of a Molecular Beam of PbF

2.1 Motivation

In this chapter, we describe and characterize a continuous beam source of lead monofluoride molecules. The importance of PbF to the measurement of the electric dipole moment of the electron (e-EDM) has been discussed in both Chapter 1 of this thesis and elsewhere [50, 7, 57, 47, 8]. The measurements of the e-EDM that we envision can not be made without a molecular beam source of PbF. Furthermore, the sensitivity of our measurement towards the electron electric dipole moment is improved by optimizing the intensity of the PbF source. The source described here allows for the spectroscopic study of PbF molecules and for testing ideas for improving the intensity of the source.

This chapter begins (section 2.2) with a review of the production of PbF molecules in the literature. Section 2.3 describes our current molecular beam source of PbF. Section 2.4 describes the characterization of our MgF_2 + PbF reactor beam source by both estimation of the rotational temperature and an analysis of molecular beam flux. Section 2.5 models the gas phase equilibrium concentration as a function of temperature in order to determine

the temperature dependence of our source and suggests dramatic improvements could be made to the beam intensity by building a higher-temperature source. Section 2.6 gives results and conclusions.

2.2 Review of Methods Used to Produce PbF Molecules

Since the 1930's, the PbF molecule has been the subject of many experimental investigations. Each of these investigations had to overcome the difficulties of creating lead monofluoride. As a heavy diatomic radical, the PbF molecule is highly reactive and only exists in thermodynamic equilibrium at very high temperature.

One of the earliest reported spectral studies of the lead halides was carried out by Howell and Rochester in 1934 [26, 63, 22]. Here emission band spectra of the PbF molecules were produced by a high frequency electrical discharge that revealed electronic structure. In 1936, Rochester improved this measurement to reveal the vibrational band spectrum of the ground X_1 and excited A states [63]. For this experiment, a successful source of PbF was made by heating lead salt (PbF_2) in a quartz 5-cm-long by 0.5-cm-internal-diameter tube. Three grams of purified lead fluoride salt was melted by heating the tube with a Bunsen burner. They were able to maintain a fairly constant vapor by continuously pumping the tube. However, it was impossible to maintain this pressure for more than two hours because of the reaction of the molten salt on the walls of the tube. The source was later replaced by a carbon-tube furnace with a temperature that could be varied from room temperature to 2000^oC [32, 64]. With this improved source Rochester was able to obtain the vibrational constants of the ($X_1,\ X_2,\ A,\ B,\ C,\ D,\ E$, and F) electronic states [64].

Morgan created PbF molecules using a similar technique of cracking PbF_2 [22]. Mor-

gan used this source to study the absorption spectra of PbF, PbCl and PbBr. Here the PbF_2 was heated in open iron or graphite tube about 30 cm in length using an electric resistance furnace. The optimal temperature for creating PbF from dissociation of PbF_2 was found to be 1500 ^{o}C. Similar techniques were used by others including R.F. Barrow for the investigation of the spectroscopic properties of the diatomic halides in 1958 [4] and for the analysis $B - X_2$, $B - X_1$, and $A - X_1$ transitions of gaseous PbF in 1976 [44]. Singh's group also cracked PbF_2 for the rotational analysis of PbF in 1968 [67]. The Barrow group observed $B - X_1$ and $A - X_1$ transitions with a 1100 K and 1300 K source respectively. Electronic $B - X_2$ transitions were observed with a source heated to 2100 K. Electronic $A - X_2$ transitions were not observed, even at a maximum temperature of 2600 K.

PbF molecules were also observed in chemiluminescence from the reaction of Pb with F_2 as $Pb + F_2 \rightarrow PbF + F$ under the beam-gas conditions at F_2 pressures of $\sim 10^{-4}$ Torr and in the presence of Argon at ~ 7 Torr by Zare's group in 1977 [14]. Here, lead (99.99 % purity) was placed inside a graphite crucible with an aperture of 0.1 cm in diameter. This system was shielded by three concentric tantalum layers. This graphite crucible was heated until the pressure reached $0.01 - 0.1$ Torr vapor pressure. A beam flux of 10^{16} atoms $\cdot$ cm$^{-1} \cdot$ s^{-1} was estimated in the reaction region for the above conditions. They observed a series of red-degraded band heads of A $^2X_{1/2} \rightarrow X_1$ $^2\Pi_{1/2}$ transitions in the wavelength regions of 400 - 540 nm. Kinetic studies were also done under the condition of oxidant pressure and metal beam flux by observing the chemiluminescent intensity to understand the dynamics of highly exothermic chemical reactions. In 1979 PbF was created by the reaction of F_2 gas with atomic Pb by Green and Davis for the direct measurements of the radiative lifetime of the A $^2\Sigma_{1/2}$ state using laser induced fluorescence [25].

Chen and Dagdigian also created PbF from the reaction of Pb with F_2 in a beam-gas scattering experiment [33]. Here the lead metal was heated to 1190 - 1250 K in graphite crucible with a orifice diameter of 0.1 cm using tantalum heater to produce ~ 1 Torr vapor pressure. The lead atoms passed into a reaction chamber through a narrow slot. A soda lime trap of F_2 was kept inside the reaction chamber. The experiment was carried out with a mixture of 5% of F_2 in He at 5×10^{-3} Torr. The PbF molecules were detected by laser fluorescence excitation using a dye laser system with a typical line width of 0.2 cm^{-1}. This fluorescence light was imaged with a telescope onto a photomultiplier. The Fink group produced PbF by flowing F_2/He and F_2/Ar gas mixtures over lead metal, where the lead was heated above its melting point ($\simeq 700K$) and reacted with the molecular fluorine for chemiluminescence studies in the near-infrared region [66]. The maximum intensity of PbF was observed with a fluorine to helium ratio of 1 : 20. In 1998, lead monofluoride was made by the Fink group using a different approach for high-resolution study of fine structure [36]. It was created by the reaction Pb vapor with the product of a cw-discharge in a NF_3/He mixture.

We note that none of these previous experimental studies explicitly mentions the role PbF might play in the measurement of the electron's electric dipole moment.

2.3 A Continuous Source of PbF Molecules

2.3.1 Overview

We have compared several continuous beam sources of PbF molecules which include (as described in section 2.3.4) a $Pb + F_2 \rightarrow PbF + F$ reactor, a $MgF_2 + Pb \rightarrow PbF$ reactor,

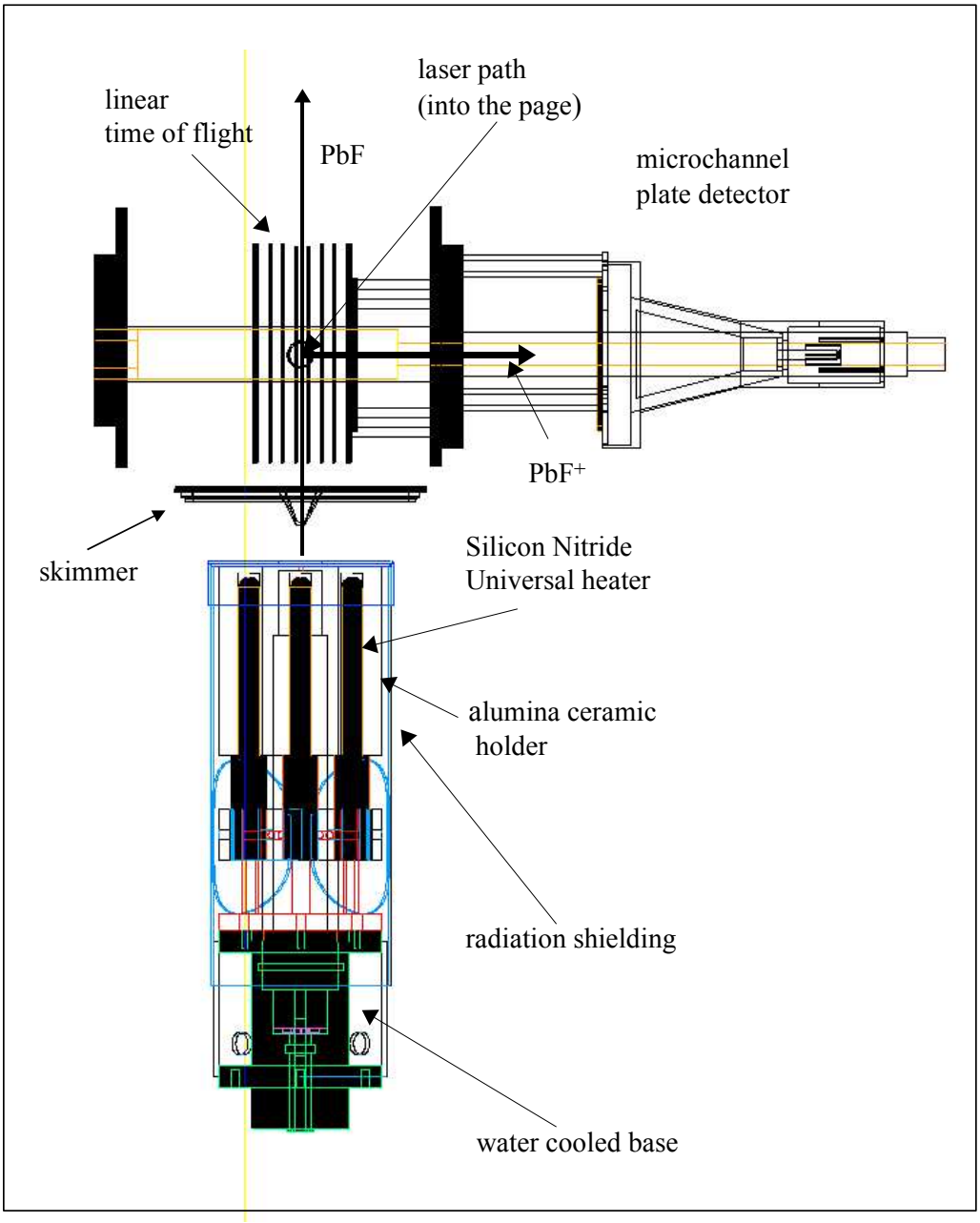

Figure 2.1: Schematic diagram of our PbF molecular beam source and detection with REMPI ionization.

a $LiF + Pb \rightarrow PbF$ reactor, and a PbF_2 cracking source. Each of these sources has been constructed using MgF_2 nozzles. This material choice was inspired by the atomic fluorine source implemented at the University of Oklahoma by Keil and coworkers[23]. MgF_2 is particularly suited to radical production because of its high melting point and because it remains chemically inert at high temperatures.

For each of our sources, we heat the MgF_2 elements to a temperature of 900°C (typical). This is achieved by surrounding the elements with an alumina ceramic block which is in turn heated with six Silicon Nitride Universal Igniters (Igniter Direct Model HSIURK120v) (Normally this type of heater is used as an igniter in ovens and other gas appliances). The alumina ceramic block is in turn surrounded by three layers of tantalum heat shields. The base of this heating system is clamped to a water-cooled mount which also serves to cool o-ring seals between the MgF_2 elements and gas inputs as shown in Figure 2.2. The temperature of the alumina ceramic block is measured with a K-type thermocouple and the temperature of the water cooled base is monitored with a resistive thermal device.

For each of our sources, inert gas enters the back of the nozzle and carries the PbF molecules with it into a high-vacuum chamber through a small exit orifice. These PbF molecules then pass through a skimmer and enter a differentially-pumped detection region. These PbF molecules are detected using resonance enhanced multiphoton ionization (REMPI). This detection of PbF molecules is described in the next two sections. Unique details of each of our attempted sources is described in section 2.3.4.

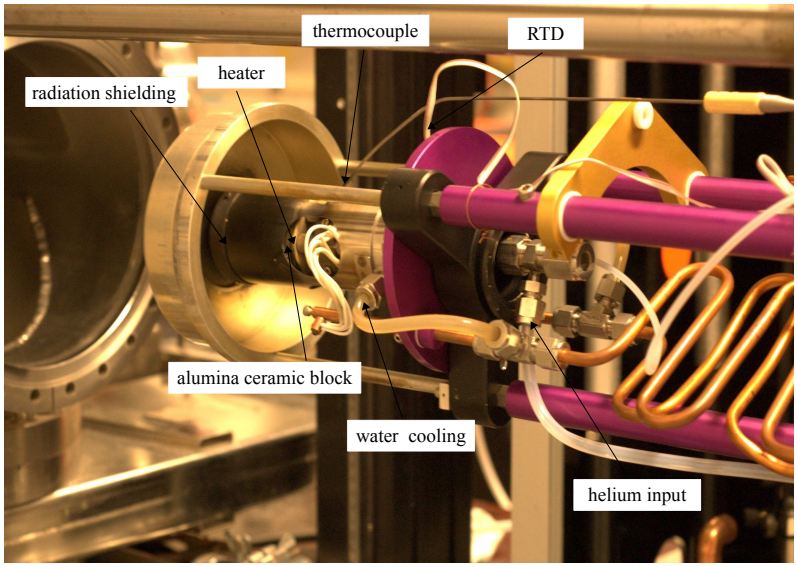

(a) Photograph of our beam source

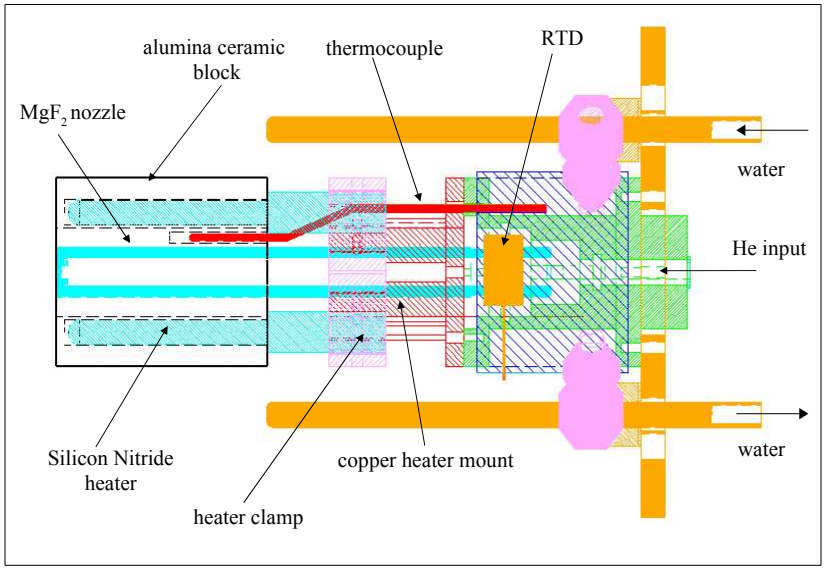

(b) Schematic diagram of our beam source

Figure 2.2: A flow reactor source of PbF molecules. The nozzle of the source is constructed from MgF_2 materials.

2.3.2 Detection of PbF Molecules

In brief, PbF molecules that enter the detection region are excited and further ionized by linearly polarized laser radiation. This laser radiation is produced by pumping a dye laser system using a 10-ns, 10-Hz Nd:YAG laser. The light is focused perpendicularly to the PbF molecular beam using a cylindrical lens. The linear time of flight (TOF) mass spectrometer shown schematically in Figure 2.1 is used to detect PbF^+ ions. These ions are produced when the laser radiation is tuned to a resonant transition of a selected ro-vibrational state. The ionization of the PbF molecules normally occurs in absence of an applied electric field. The ions then are accelerated by applying a 700 volt pulse to extraction plates spaced by 27.3 mm. The 250-ns (typical) delay of this pulse with respect to the laser ionization as well as the 1.3 μs (typical) duration of the pulse are taken to optimize the mass resolution of the time of flight [70]. After leaving the extraction region, the ions travel through a field free region and reach a microchannel plate detector. The time delay from the application of the 700-volt pulse to detection allows for mass discrimination as shown by the mass spectrum collected using a Tektronics (TDS3034) digital oscilloscope and shown in Figure 2.12.

In summary, this detection scheme allows us to detect (with $\sim 40\%$ efficiency) all PbF molecules in a given ro-vibrational state that exist in a $0.04 \times 1. \times 3.$-mm^3 (typical) detection volume with a repetition rate of 10 Hz. Furthermore, we are able to simultaneously collect and separate the signal for each of the common isotopes of PbF.

We have employed several different REMPI schemes to ionize PbF molecules [7, 57]. Most of the data presented in this chapter are collected using 1+1 REMPI. For this scheme 280-nm laser radiation is used to drive the B $^2\Sigma_{1/2} \leftarrow$ X$_1$ $^2\Pi_{1/2}$ transition. This laser

radiation is produced by second harmonic generation (SHG) of the 560-nm output of our dye laser in a BBO crystal. After excitation by 280-nm laser radiation, 355-nm laser radiation ionizes the B-state. This 355-nm light is produced by third harmonic generation (THG) of the 1064-nm output of our Nd:YAG laser. This multiphoton ionization scheme made it possible to determine rotational temperature of our source (as described in section 2.4.1), evaluate the output flux of our source (as described in section 2.4.2) and, when the 355-nm laser radiation is replaced with a tunable laser, measure the ionization threshold of the PbF molecule (as described in section 2.3.3 and reference [7]).

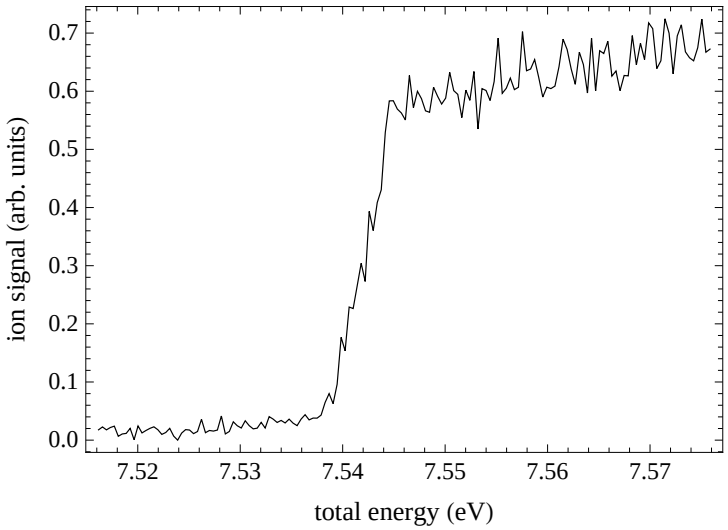

Figure 2.3: Threshold ionization of PbF molecules via REMPI of B-state at total energy 7.54(1) eV [7]

2.3.3 The Ionization Potential of PbF

We determine the ionization potential of the PbF molecule by tuning the pump laser radiation (35689 cm^{-1}) at the band head of $X_1\ ^2\Pi_{1/2} \leftarrow B\ ^2\Sigma_{1/2}$ transition and scanning the wavelength a second source of ionizing laser radiation. The appearance ionization energy is shown in Figure 2.3. We confirm that this appearance ionization is due to the ground-state ion by scanning the probe laser 1800 cm^{-1} to the red without observing ions. We conclude the ionization potential of $^{208}Pb^{19}F$ is 7.54 ± 0.01 eV [7]. This value is consistent with a previous measured value of 7.5 ± 0.3 eV [37].

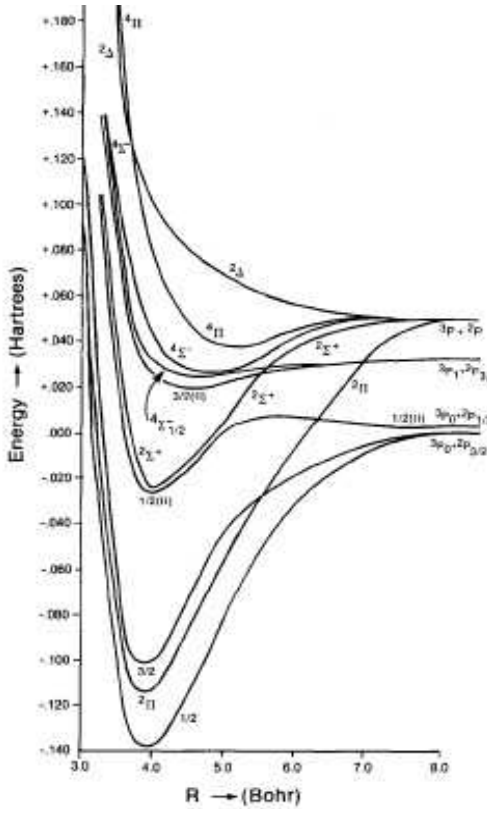

Figure 2.4: Electronic energy levels based on the calculation of reference [34]

In a second study we verify this measurement by employing a three-photon 1+1+1 REMPI scheme resonant with both the A $\leftarrow$ X1 and D $\leftarrow$ A transitions. Excitation from the X_1 to the A state occurs at 436.612 nm corresponding to an R-branch pileup. This radiation excites roughly 5 rotational states centered about $J = 23/2$. A second laser tuned to 476.6 nm further excites these PbF molecules to the D state. These D-state molecules are then ionized by tunable laser radiation at 590 nm revealing an appearance ionization. This appearance ionization occurs at a total energy of 7.55 ± 0.01 eV, consistent with the two-photon observation [57].

2.3.4 Our Beam Source of PbF Molecules

At the early stages of our experimentation with PbF , we followed methods of the Fink group [66]. Specifically we produced PbF by the reaction of lead vapor with fluorine. The greatest engineering challenge of this source was to create a region where fluorine gas would react with lead vapor while, at the same time, not coming in contact with the molten lead producing the Pb vapor. To meet this challenge, we developed a triaxial MgF_2 nozzle system. A machine drawing of this source is shown in Figure 2.5. The MgF_2 nozzles are radiatively heated to $900 - 1000^{o}$C. Helium entering the back of the intermediate nozzle passes over molten lead (99.99% purity, SigmaAldrich) and carries the lead vapor with it to a reaction region created by the outer nozzle. At the same time, a 1 : 20 gas mixture of F_2 and He reaches the reaction region through the inner nozzle. The F_2 and Pb mixture in the reaction region creates PbF which flows into the source chamber.

In the best case, the lead pellet lasted around 10 hours. More often than not, the molten lead was fluorinated in a much shorter time, stopping the production of PbF molecules after

only one or two hours. This first generation (triaxial) source was abandoned due to the high frequency with which this fluorination event required us to follow a complicated procedure for reloading the lead pellet. This procedure led to many delays and frequent breakage of the MgF_2 components.

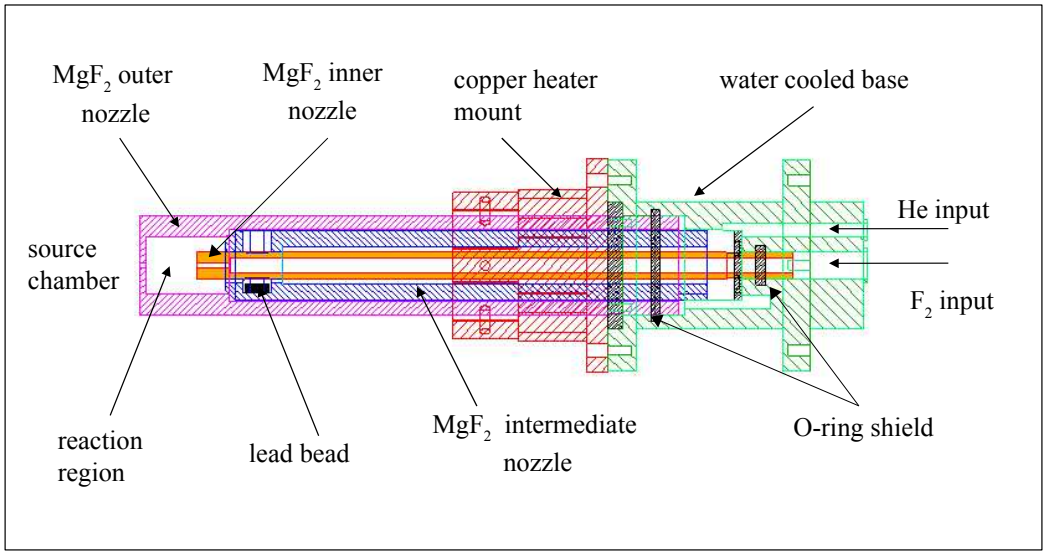

Figure 2.5: The schematic diagram of first generation of PbF flow reactor source. Here F_2 and He mixing flows through MgF_2 inner nozzle and lead vapor is carried by Helium in MgF_2 intermediate nozzle. The reaction of Pb and F_2 happens in the reaction region.

Our second source replaced the triaxial design with the coaxial design shown in Figure 2.6. Here the F_2/He gas mixture flows directly into a reaction region created by the MgF_2 outer nozzle. The MgF_2 inner nozzle contained a small amount of molten lead which was kept at the front of the tube by tilting the entire source slightly. Helium gas passed over this molten lead and into the reaction region, carrying lead vapor with it. This lead vapor

combined with the fluorine gas to produce PbF molecules which entered the source region. The partial pressure of the inner nozzle was kept large enough to prevent the fluorine from effusing back into the inner nozzle. The performance of this second-generation source (both in terms of output and operating time) was similar to our first source. However, it proved much easier to clean and reload.

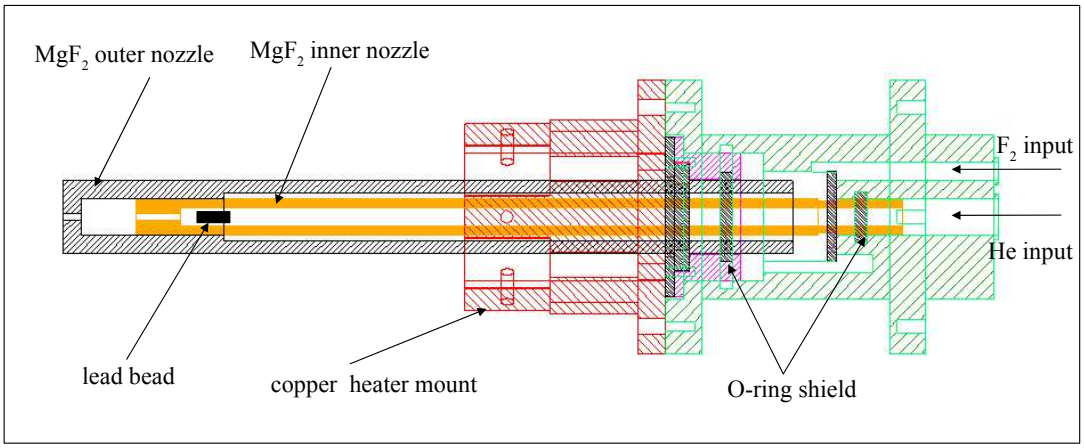

Figure 2.6: The schematic diagram of second generation of PbF flow reactor source. Here, Helium flows through MgF_2 inner nozzle and F_2 flows through MgF_2 outer nozzle and the entire source was slightly tilted to keep the molten lead in the front of the nozzle.

Our third generation source was brought about by the serendipitous discovery that PbF molecules could be produced without any fluorine gas. This occurs because PbF molecules are created by the reaction of lead vapor and the nozzle surface of the MgF_2 material. This discovery led to the rapid development of a simple and reliable single-nozzle MgF_2 reactor. This third - generation source is designed with a small reservoir to contain molten lead

that is kept near its 0.2-mm diameter exit orifice (Figure 2.3.4). The reservoir is made by grooving a $3 \times 3 \times 30-\text{mm}^3$ block of MgF_2. The nozzle is heated to 900 ^{o}C and PbF molecules created from the $MgF_2 + Pb$ reaction are carried into the source chamber by helium that flows from the back of the nozzle. The intensity of the output is approximately a factor of 2 smaller than the $F_2 + Pb \rightarrow PbF + F$ reactor. However, the source consistently produces PbF molecules for over fifteen hours. Furthermore, the source is simple to handle and recharge after the molten lead evaporates. This reliable source has allowed us to carry out a multitude of spectroscopic studies [7, 8, 57, 58].

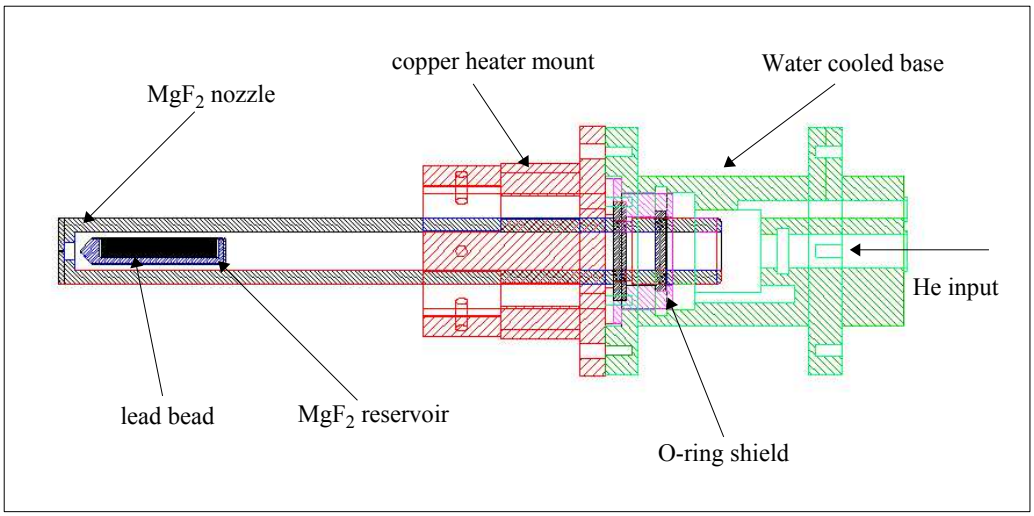

Figure 2.7: The schematic diagram of third generation of PbF flow reactor source. Here, a small reservoir contain molten lead and Helium flow through the back end of the nozzle and carrying the PbF with it.

After development of the MgF_2 reactor, a few other strategies were attempted. In one

study, we used a lithium fluoride reservoir to create PbF molecules. We were able to produce PbF molecules, but a reaction of the LiF and MgF_2 caused the MgF_2 nozzle to shatter. We hypothesize that this shattering was caused by a crystal structure difference between the LiF and MgF_2. We also used PbF_2 powder in a reservoir and a MgF_2 nozzle to create the PbF. PbF molecules were observed at a temperature of 750°C. Unfortunately, the PbF_2 clogged the nozzle in a matter of minutes. In the end, the reliability and reasonable intensity of the $MgF_2 + Pb$ reactor made it the production method of choice. In the next section we describe the characterization of this source.

2.4 Characterization of Our $MgF_2 + Pb$ Beam Source

We have characterized both the rotational temperature and molecular beam flux of our MgF_2 reactor source. We are able to measure the rotational temperature of our source by fitting our observed B $^2\Sigma^+_{1/2}(v' = 0) \leftarrow$ X$_1$ $^2\Pi_{1/2}(v'' = 0)$ spectra. These measurements are described in detail in this section.

2.4.1 Rotational Temperature of the PbF Source

To analyze the B $^2\Sigma^+(v' = 0) \leftarrow$ X$_1$ $^2\Pi_{1/2}(\ v'' = 0)$ spectra of PbF, we consider the energy of a state of the PbF molecule as a sum of rotational, vibrational and electronic energies. Then we consider the allow dipole transitions between the upper and lower rovibronic states.

Quantum numbers of the upper state indicated by primes (e.g J') and lower state indicated by double primes (e.g J''). The energy of the ground X$_1$ state of our PbF molecule is assumed to be that of a symmetric top with Ω-type doubling[29, 24]:

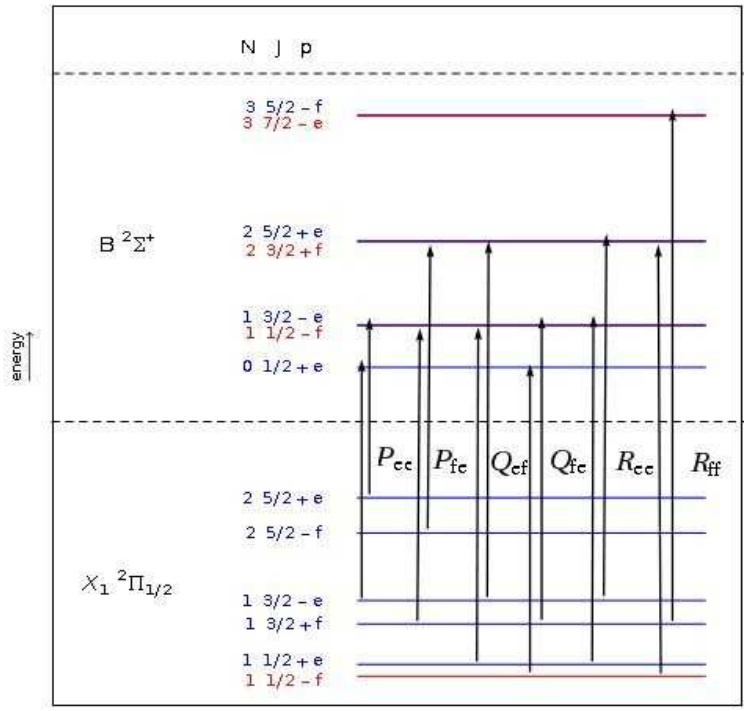

Figure 2.8: Energy level diagram for the first few lines of $B^2\ \Sigma^+(v' = 0) \leftarrow X_1\ ^2\Pi_{1/2}(v'' = 0)$ transition. The possible six branches are designated by P_{ee}, P_{ff}, Q_{ef}, Q_{fe}, R_{ee} , and R_{ff}.

$$F_{X_1}(J^{''}, P^{''}) = B^{''}J^{''}(J^{''}+1) - D^{''}(J^{''}(J^{''}+1))^2 + \frac{\Delta^{''}}{2}P^{''}(-1)^{J^{''}-1/2}(J^{''}+1/2) \quad (2.1)$$

Here, $J^{''}$ is the rotational quantum number, B'' is the rotational constant, D'' is the centrifugal distortion, $P'' = \pm 1$ is the total electronic parity, and $\Delta^{''}$ is the Ω-doubling constant of the ground state. The energy of the excited $B\ ^2\Sigma_{1/2}$ state is expressed below:

$$F_B(J^{'}, P^{'}) = B^{'}J^{'}(J^{'}+1) - D^{'}(J^{'}(J^{'}+1))^2 + \frac{\Delta^{'}}{2}P^{'}(-1)^{J^{'}-1/2}(J^{'}+1/2) + T^{'}_{oo} \quad (2.2)$$

Here, $J^{'}$ is the rotational quantum number, B' is the rotational constant, D' is the cen-

trifugal distortion, P' is the total electronic parity, $\Delta^{'}$ is the Ω-doubling constant, and T'_{oo} is the energy of the lowest rovibronic state of the B state. (The Ω-doubling constant Δ' for a $^2\Sigma$ state is related to the more usual spin doubling constant γ by $\Delta' = \gamma' - 2B'$. See [39].) Values for all but T'_{oo} are taken from reference [44]. These values (in units of cm^{-1}) are $B'' = 0.228027$, $D' = 1.852 \times 10^{-7}$, $\Delta^{'} = -0.1382$, $B'' = 0.24736$, $D^{''} = 1.62 \times 10^{-7}$, and $\Delta^{''} = -0.497$. The electronic energy $T_{oo} = 35720.\ \mathrm{cm}^{-1}$ is taken from unpublished results in our laboratory.

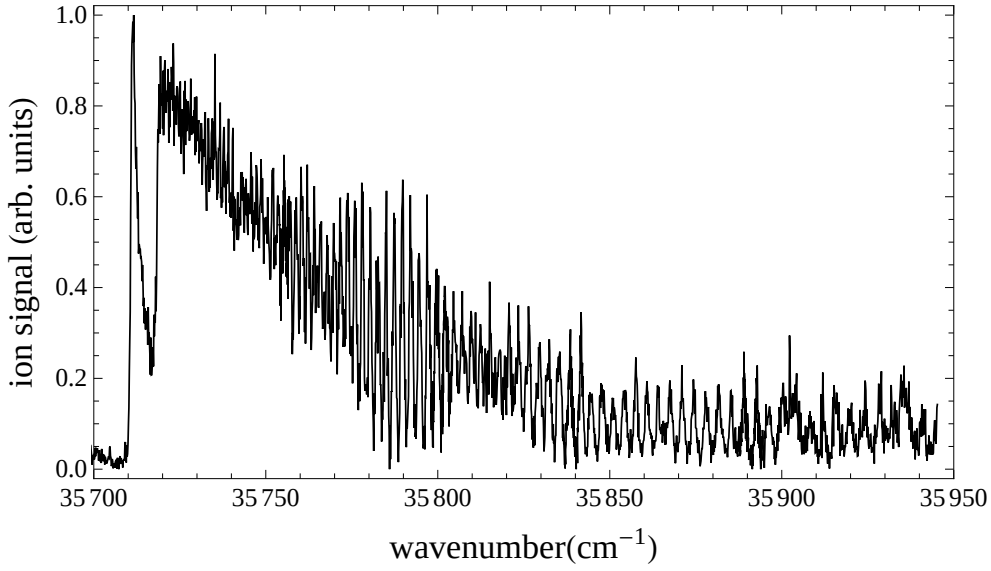

Figure 2.9: Observed spectrum of $\mathrm{X}_1\ ^2\Pi_{1/2}(v=0) \leftarrow \mathrm{B}\ ^2\Sigma^+_{1/2}(v=0)$ of PbF molecule from our $\mathrm{MgF_2} + \mathrm{Pb}$ reactor source.

The allowed dipole transitions are those parity-changing transitions for which $\Delta J = 0,\ \pm 1$ and $\mathrm{P}'\ \mathrm{P}'' = -1$. Transitions for which $\Delta J = J^{'} - J^{''} = -1$ belong to the P-branch, $\Delta J = J^{'} - J^{''} = 0$ belong to the Q-branch, and $\Delta J = J^{'} - J^{''} = 1$ belong to the R-branch.

It is convention to designate those rotational levels with a total parity $P = +(-1)^{J-1/2}$ as e parity and designate those rotational levels with a total parity $P = -(-1)^{J-1/2}$ as f parity states [6]. By this convention, the energy ordering of the e and f state is the same for each rotational state. For this scheme Q-branch $e \leftrightarrow f$ and $f \leftrightarrow e$ transitions are allowed whereas for P and R branches $e \leftrightarrow e$ and $f \leftrightarrow f$ transitions occur (Figure 2.8). To designate the parity of the excited and ground state, two subscripts are added to the branch designation. Thus the six branches P_{ee}, P_{ff}, R_{ee}, R_{ff}, Q_{ef}, and Q_{fe} are observed. We note for clarity that, for the Q_{ef} state, the total parity of the excited state is e (i.e., $P' = (-1)^{J'-1/2}$) and the total parity of the ground state is f (i.e., $P'' = -(-1)^{J''-1/2}$).

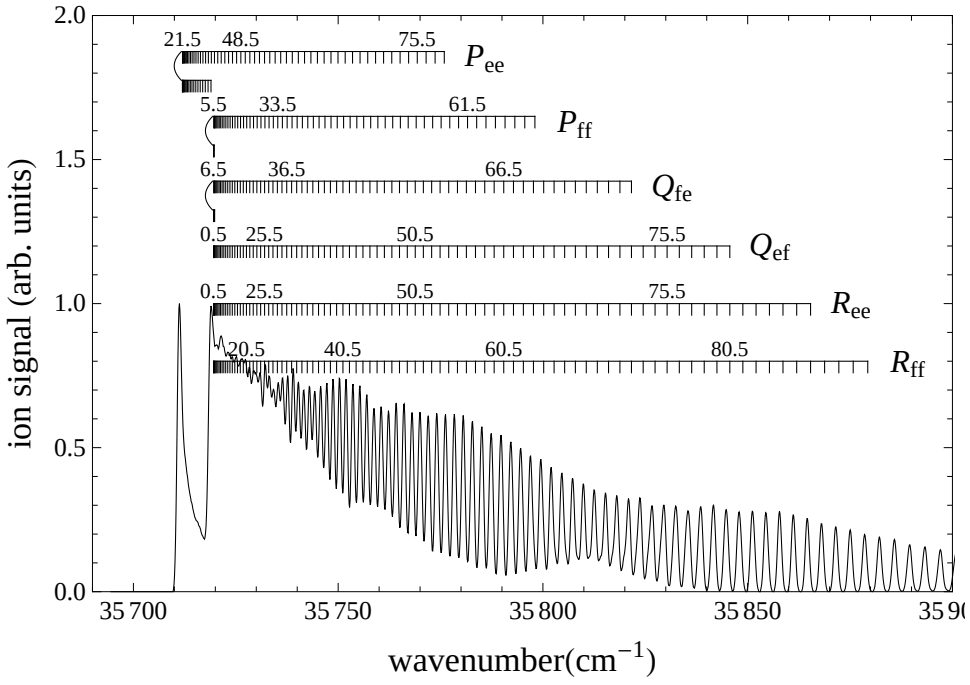

Figure 2.10: The simulated spectrum at 1000 K and constants are obtained from reference [44]. The double turn around pileup are created from P-branch and Q_{fe}-branch.

The thermal distribution of the rotational levels is needed to determine the intensity of each transition. This population is given by a Boltzmann distribution:

$$P(J^{''},P^{''}) = \frac{(2J^{''}+1)\ \exp(-F_{X1}(J^{''},P^{''})/k_BT)}{\sum_{J_i^{''},P_i^{''}}((2J_i^{''}+1)\ \exp(-F_{X1}(J_i^{''},P_i^{''})/k_BT))} \tag{2.3}$$

Here k_B is the Boltzmann constant and T is the rotational temperature of the molecule. The spectrum of rovibronic states of molecules is then given by:

$$S(\nu) = \sum_{J^{''}P^{''},J^{'}P^{'}} P(J^{''},P^{''})S_{J^{'},P^{'},J^{''}P^{''}}\ \exp\left[\frac{-4\ ln2(\nu_{laser}-\nu_{J^{''}P^{''},J^{'}P^{'}})^2}{\Delta\nu^2}\right] \tag{2.4}$$

where

$$\nu_{J^{''},P^{''},J^{'},P^{'}} = \frac{F_B(J^{'},P^{'}) - F_{X_1}(J^{''},P^{''})}{h} \tag{2.5}$$

is the transition frequency and $S_{J^{'},P^{'},J^{''}P^{''}}$ is the relative transition dipole moment. Lumley and Barrow have determined that the $X_1 \leftarrow B$ transition dipole moments are well approximated by the assumption that the transition dipole is perpendicular to the bond axis[44]. For this case we may make the simplifying approximation that $S_{J^{'},P^{'},J^{''}P^{''}} = 1$ for R_{ee}, R_{ff}, P_{ee} and P_{ff} branches ($|J' - J''| = 1$) and $S_{J^{'},P^{'},J^{''}P^{''}} = 2$ for the Q_{ef} and Q_{fe} branches ($J' = J''$) [29].

Figure 2.10 gives the simulated spectra of Eq 2.4. It is in good agreement with the experimental data of Figure 2.9. Note that the spectra features a sharp cut off in intensity at the lowest transition frequency and a gradual loss of intensity with increasing frequency. Such a spectrum is called *blue-degraded*. To understand these features, we note that (ignoring the very small contribution proportional to the constant D) the difference between the energy of Eq 2.2 and Eq 2.1 (i.e., the transition energy) is quadratic in the rotational quantum number J'' regardless of whether one is observing a P, Q, or R transition (i.e., independent of the condition $J' = J'' - 1$, $J' = J''$, or $J' = J'' + 1$). Furthermore, the

quadratic coefficient of the transition frequency as a function of J'' is $B' - B''$. Because $B' > B''$, the spectra is blue degraded. The sharp turn around occurs when the term linear in J'' is of the opposite sign of the quadratic term. From the transition energy designations in Figure 2.10, we see that this occurs for the P_{ee}, P_{ff}, Q_{fe} and R_{ff} branches.

Temperature-dependent fits to the experimentally obtained spectra are given in Figure 2.10. To obtain a temperature that is not sensitive to the precise values of spectroscopic constants or the experimental resolution, both simulation and experimental data are smoothed before fitting. We obtain good agreement between our simulated spectra and experimental data at a rotational temperature at 1000 ± 50 K (see Figure 2.11). This value is in agreement with source temperature of 950^oC as measured with a thermocouple gauge.

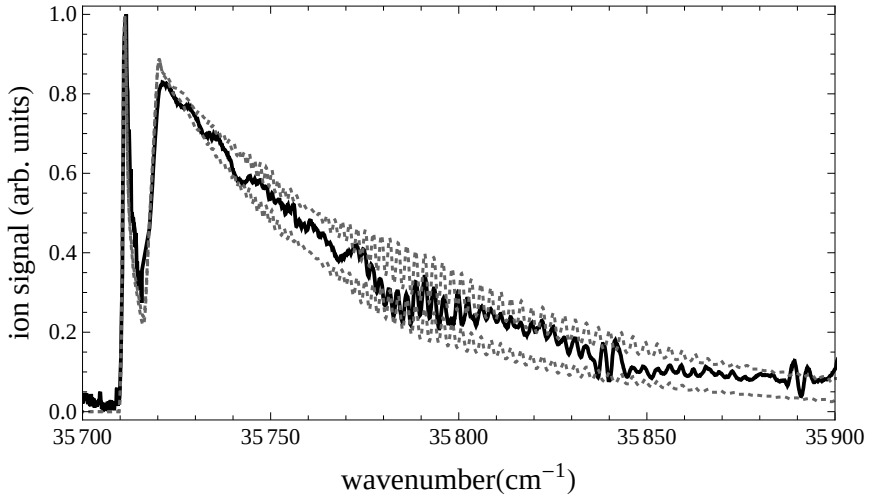

Figure 2.11: Solid line : Absorption spectrum of $X_1 - B$ of PbF, The simulated spectrum are dashed line at 1000 ± 200 K.

We note that, although we resolve rotational structure for $J'' > 80.5$, the short lifetime of the B state does not allow us to resolve lower rotational levels. This shortcoming is due to the short lifetime of the B state of PbF. This led to the development of double-resonant enhanced ionization of the molecule via the long lived A state and the short lived D state of the molecule. This scheme has been briefly introduced in section 2.3.3 and is described in detail in the following chapters of this thesis.

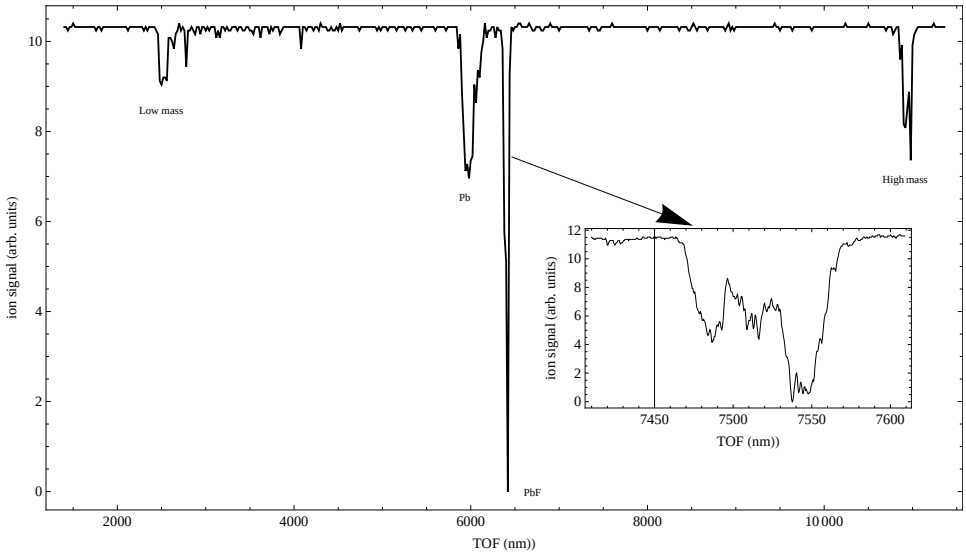

Figure 2.12: One of the first time-of-flight spectra taken of PbF taken in our laboratory. The three peaks in the inset correspond to $^{206}Pb^{19}F$, $^{207}Pb^{19}F$, and $^{208}Pb^{19}F$. Further improvements to the system have led to base-line resolution of these isotopomers.

2.4.2 The Molecular Flux of Our Source

The flux of our molecular beam source is determined by analysis of the ion production rate, geometry of our detection scheme and the efficiency of our detection. In Appendix A.1 we show that the flux (particles per quantum state per strrad) of an effusive molecular source can be expressed as:

$$\frac{d\Gamma}{d\Omega} = \overline{v}\rho_{source}A_{source} \tag{2.6}$$

$$= 4\pi\overline{v}\rho_t R^2 \tag{2.7}$$

In the first of these expressions, ρ_{source} is the density of particles in the source, $\overline{v} = (\frac{8k_BT}{\pi m})^{1/2}$ where it is referred as average velocity of the particles at temperature T, and A_{source} is opening of the source. In the second of these expressions, ρ_t is density of particles in the detection volume and R is distance between source orifice and the ionizing laser radiation. This second expression is useful because we can determine ρ_t experimentally. The ionization signal we observed is related to the density of PbF molecules in the ionization volume by

$$\rho_t = \frac{\text{Sig}}{V_{ion}S_o}\frac{1}{\epsilon} \approx 1 \times 10^5 \text{ cm}^{-3} \tag{2.8}$$

$$\rho_s = \rho_t\frac{4\pi R^2}{A_{source}} \tag{2.9}$$

$$= 5 \times 10^{10}\frac{molecules}{cm^3 \cdot quantum\ state} \tag{2.10}$$

Here Sig is the observed integrated ionization signal and S_o the integrated single ion integrated signal, V_{ion} is ionization volume and ϵ is efficiency of our detector. The estimate is approximate because of day to day fluctuation in signal intensity of as much as an order of magnitude. The value for ρ_t above is taken from an assumed ionization volume of

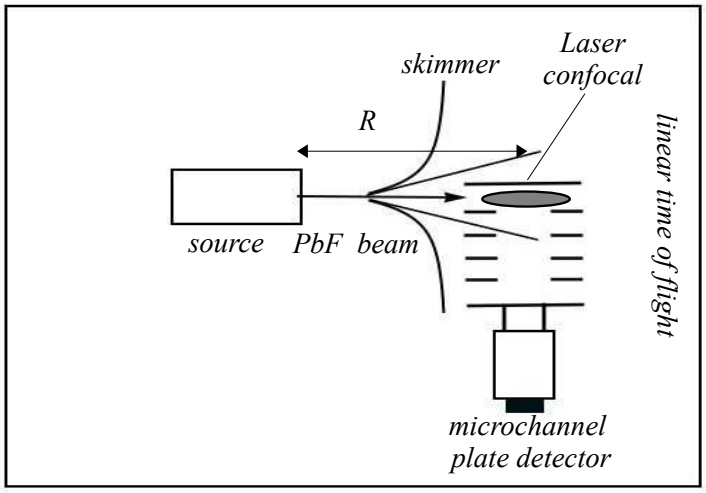

Figure 2.13: Geometry of our beam source detection scheme.

$(0.04 \times 1 \times 3)$ mm^3, a ratio Sig/S_o of 10 ions, and an efficiency $\varepsilon = 0.5$. From this estimate for ρ_t, a source-detection distance $R = 10$.cm, and a mean velocity of 350 cm/sec, one finds

$$\frac{d\Gamma_{\exp}}{d\Omega} \approx 1 \times 10^{11} \frac{molecules}{strrad \cdot \sec \cdot quantum\ state}. \tag{2.11}$$

By equating Eq 2.6 to Eq 2.7 we can related the density in the source to the density of particles measured in the detection region:

$$\rho_s = \rho_t \frac{4\pi R^2}{A_{source}} \tag{2.12}$$

$$= 5 \times 10^{10} \frac{molecules}{cm^3 \cdot quantum\ state} \tag{2.13}$$

Given the fact that approximately 6000 rotational states are populated at 1000 K, this corresponds to a total density of 3×10^{13} PbF molecules/cm^3 in our source. In the next sec-

tion, we create a thermodynamic model to attempt to predict the density of PbF molecules in the source. Our motivation is both to confirm our experimentally obtained estimate of 3×10^{13} molecules/cm^3 and suggest possible improvements that could be made to increase the beam flux.

2.5 Prediction of Thermal Equilibrium Concentration of PbF in a Pb/F_2 source

Although thermodynamically stable at high temperatures, the PbF radical is expected to be highly reactive and easily quenched by reaction with the walls of the nozzle and other contaminant species. Here we develop a thermodynamic model of the concentration of PbF molecules in our source. By comparing the predicted density of molecules from thermodynamics to the 3×10^{13} molecules/cm^3 estimated in the previous section, we can access if reactive losses due to impurities in our system is occurring. We have produced roughly equally intense sources of PbF from a $MgF_2 + Pb$ reactor at 1300 K, by mixing hot F_2 gas with Pb vapor at 1200 K, and by cracking PbF_2 at 1000 K. Thermodynamic constants have been determined by others that enable us to predict the partial pressure of PbF in the $Pb + F_2$ flow reactor and the PbF_2 cracking scheme.

To determine the concentration of PbF in our source, we must balance reactions pro-

ducing F_2, Pb_2, PbF_2, PbF_4 :

$$2F \rightleftharpoons F_2$$

$$2Pb \rightleftharpoons Pb_2$$

$$2F + Pb \rightleftharpoons PbF_2$$

$$4F + Pb \rightleftharpoons PbF_4$$

We assume that other species do not occur in significant quantities at the high temperature of our source.

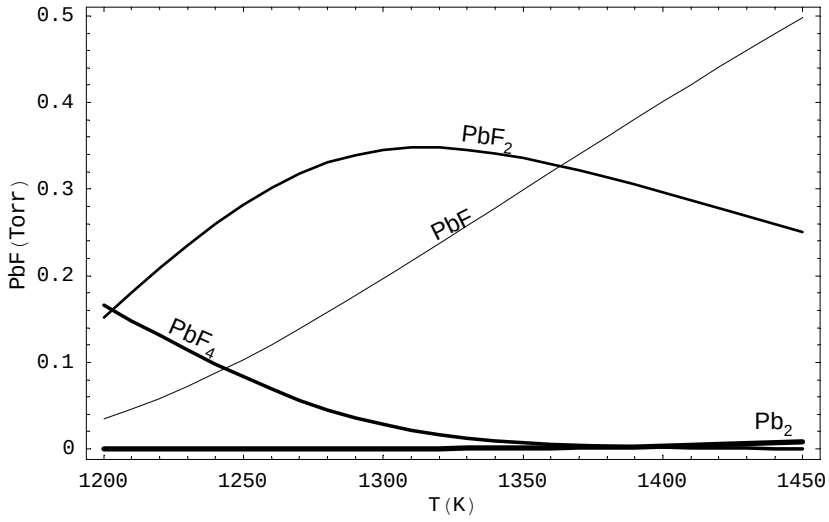

Figure 2.14: Expected partial pressure of Pb, Pb_2, PbF, Pb_2, and PbF_4 as in the Pb + F_2 flow reactor as a function of temperature.

The equilibrium constant of K for each $n_A A + n_B B \rightarrow n_C C + n_D D$ processes is defined by

$$K = \frac{P_C^{n_C} P_D^{n_D}}{P_A^{n_A} P_B^{n_B}} = e^{-\Delta G/RT} \tag{2.14}$$

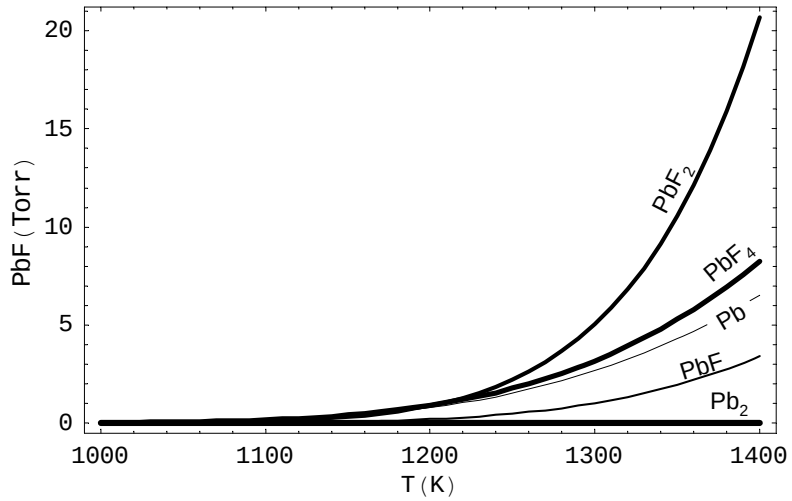

Figure 2.15: Expected partial pressure of Pb, Pb_2, PbF, Pb_2, and PbF_4 as in the PbF_2 cracking source as a function of temperature.

where ΔG is the change in Gibbs free energy with $G = H - TS$ where H is the enthalpy and S the entropy in each species. The temperature dependent entropy and enthalpy in turn is obtained by evaluating Eq 2.15 and 2.16, using parameters available in the National Institute of Standards Chemical Web book [1].

$$H - H^\circ = AT + BT^2/2 + CT^3/3 + DT^4/4 - E/T + F - H \tag{2.15}$$

$$S^\circ = A \ln T + BT + CT^2/2 + DT^3/3 - E/(2T^2) + G \tag{2.16}$$

To model our flow reactor, we estimate a partial pressure of 2 Torr of F_2 enters the flow region. We also assume that the partial pressure of Pb atoms is given by the vapor pressure of lead at the temperature of the source. These two conditions, as well as the four

equilibrium conditions of the form of Eq 2.14 allow us to solve for the partial pressure of each atom and molecule as a function of temperature. The partial pressure of PbF at 900^{o}C is seen to be 0.035 Torr corresponding to a density of 3.3×10^{14} PbF molecules/cm^3.

To model the production of PbF molecules from the direct cracking of PbF_2, we assume atomic number densities corresponding to published vapor pressure curves for the PbF_2 molecule [10]. When these number densities are assumed, we find an expected concentration of 3×10^{13} PbF molecules/cm^3 in the nozzle.

Given the order-of-magnitude nature of our experimental determination of the source density, both our model of the flow reactor and PbF_2 cracking source are in reasonable agreement with experimental observation. For both the flow reactor and cracking sources, we predict a dramatic increase in source density (from millitorr to torr) when the source temperature is increased beyond the melting point of the MgF_2 walls of our current source. Development of new sources made from other alternative materials is ongoing in the laboratory.

2.6 Summary

We have developed a molecular beam source suitable for spectroscopic studies of the PbF molecule. The rotational temperature of PbF molecules is found by fitting B $^2\Sigma^+_{1/2}(v' = 0) \leftarrow$ X$_1$ $^2\Pi_{1/2}(v'' = 0)$ transition with experimental data and found it to match the temperature of the nozzle. We have measured the ionization potential of the molecule by observing appearance ionization from both the B and D states of the molecule. Finally, we have determined an estimate of the number density of PbF molecules in our source that compares favorably to that expected from a thermodynamical model. This

model suggests that a much brighter source of PbF molecules could be made by increasing the temperature of the source.

Chapter 3

Direct measurement of a picosecond lifetime with a nanosecond laser: Application to Lifetime of the D state of PbF

3.1 Introduction

3.1.1 Overview

This chapter demonstrates a method of measuring the short-lived (subnanosecond) lifetime of the D state of the PbF molecule using a 10-ns Neodymium-doped yttrium aluminum garnet (Nd:YAG) laser system. To accomplish this measurement, we employ an intensity autocorrelation technique normally used to measure the time profile of ultra-short laser pulses. We compare this measurement to an estimate of the lifetime the spectral linewidth of an observation of the D $\leftarrow$ A transition.

This chapter is organized in the following manner: Section 2.1 presents why the lifetime of D state is important to the design of an efficient ionization scheme of the PbF molecule. Section 3.1.3 surveys lifetime measurements of excited states of atoms and molecules using

optical-excitation methods. Section 3.1.4 explains principles of intensity autocorrelation methods. Section 3.2.1 outlines the laser radiation and ionization scheme for the PbF molecule and Section 3.2.2 presents experimental details of our autocorrelation measurement. Section 3.3 presents our data analysis and section 3.4 gives results and conclusion. The data presented in sections 3.2- 3.4 appeared in a recent publication in the Physical Review A [57].

3.1.2 Motivation

As discussed in Chapter 1, heavy paramagnetic radicals are expected to be 1000 to 10,000 times more sensitive to an e-EDM than atoms [27, 39]. However, there is a problem that has prevented molecular e-EDM measurements from surpassing the limit of atomic measurements. Specifically, the reactivity of heavy radicals and state dilution make it difficult to achieve an intense flux of ground-state molecules. One way to compensate for this problem is by increasing the sensitivity of the detection method employed in the experiment.

Previous e-EDM experiments using atoms [17, 49] and molecules [27] have employed laser induced fluorescence (LIF) detection. In our present detection scheme we have replaced LIF with resonance enhanced multiphoton ionization (REMPI). Here, laser light is focused into the molecular beam exciting those PbF molecules in a state which we wish to observe. In an LIF-based measurement, these excited molecules would emit a photon that is then detected by a photomultiplier tube. To avoid scattered light, only a small fraction of emitted photons (typically 0.1%) are observed. In our REMPI scheme, these

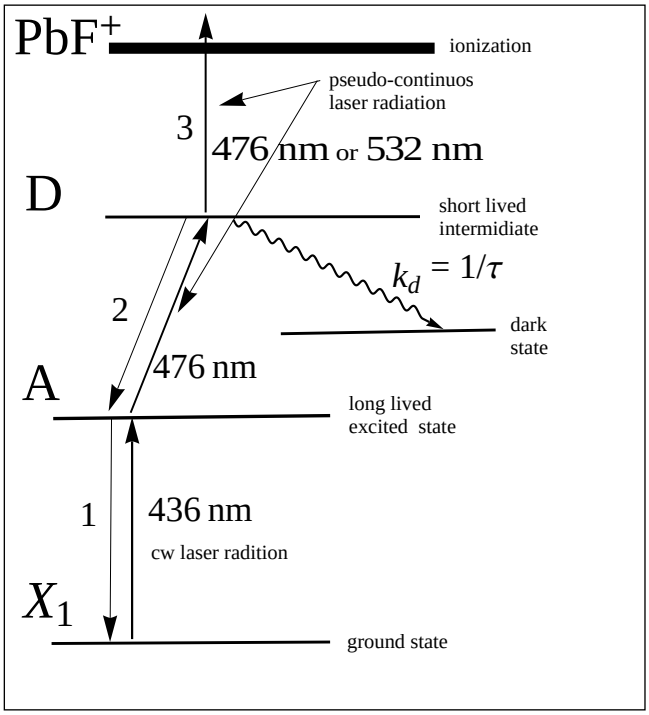

Figure 3.1: Schematic level diagram of $^{208}Pb^{19}F$ molecule for doubly resonant rotational state sensitivity ionization scheme.

excited molecules are further excited to ionization and accelerated to a microchannel plate detector. The sensitivity of the REMPI technique surpasses that of an LIF technique by both increasing the fraction of excited molecules that are detected and by allowing for mass discrimination. In a pulsed laser detection scheme, the technique of resonance enhanced multiphoton ionization (REMPI) is typically 100 to 10,000 times more sensitive than LIF [20].

Our initial achievement of REMPI of PbF was carried out with a 10 Hz, 10 ns Nd:YAG-pumped dye laser system. Although this system was ideal for exploring possible ionization schemes, its 10 Hz repetition rate led to an effective duty cycle of 10^{-4}. To achieve the

increase in sensitivity that REMPI allows over other techniques, this low duty cycle must be overcome by replacing the 10-Hz laser system with either a continuous or pseudo-continuous source of laser radiation.

For the case of continuous radiation, molecules are ionized by a continuous source of laser radiation. For the case of pseudo-continuous ionization, a pulsed laser with a very high repetition rate (76-100 MHz typical) is used to drive the ionization step. Such pulsed lasers are available with pulses that are sub-femtosecond to hundreds of picoseconds in duration. The technology of the laser system changes dramatically between continuous, femtosecond and picosecond pulse durations. The appropriate choice of technology requires knowledge of the lifetime of the intermediate D state.

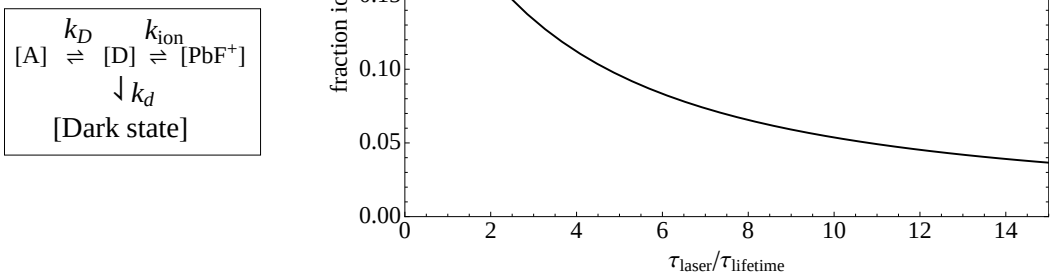

(a) (b)

Figure 3.2: (a) A rate equation used to determine the source of laser radiation and lifetime of the D state and (b) Ionization signal as the pulsed width of laser radiation of steps 2 and 3 in Figure 3.1.

To understand the importance of the D-state lifetime, we consider Figure 3.1 that illustrates the doubly resonant ionization scheme which we found to efficiently ionize the PbF molecule. Here the A-state lifetime ($\tau > 1\mu$s [33]) is much longer than the time it takes for a PbF molecule to cross a focused laser beam(approx 20ns). For this reason, a continuous source of diode laser radiation may be employed to excite the A $\leftarrow$ X1 transition. In the analysis we present here, we need only consider the kinetics of driving the D state to ionization. A short D-state lifetime prevents this process from being driven by a truly continuous source of laser radiation: If the D state decays rapidly, the chance of absorption of the final photon required for ionization becomes vanishingly small. To quantify this point, we consider the case that the excitation steps 2 and 3 shown in Figure 3.1 are excited by a pseudo-continuous source of laser radiation made up of pulses of duration ΔT. The rates of excitation k_D and K_{ion} are proportional to the intensity of laser radiation. We assume that we are able to achieve a time integrated intensity(fluency) per pulse so that $k_D \Delta T = k_{ion} \Delta T = 2$. A simple rate model can then be used to determine the fraction of D-state PbF molecules ionized by each pulse of laser radiation. Figure 3.2(b) shows this fraction as a function of the ratio $\Delta T/\tau$. From this plot we see that, to achieve efficient ionization, the pulse duration must be less than or approximately equal to the lifetime of the D state.

Our realization of this requirement presented a challenge: Specification of a new laser system to drive the ionization step required knowledge of the D state. Although it was obvious (from delayed ionization experiments) that the lifetime of the D state was under 7ns, we did not know how much under. Unfortunately, observed spectral lines of the D $\leftarrow$ A transition roughly matched the bandwidth of our 10 Hz laser system ($\simeq 0.2 - cm^{-1}$). For

this reason it was impossible to determine a reliable linewidth and deduce the lifetime. This chapter describes how we used autocorrelation techniques to coax our 10-ns system into making a direct measurement of the D state lifetime.

3.1.3 Lifetime-Measurements Using Optical Excitation

In this section, we present a brief history of methods for measuring the lifetimes of the excited-levels of atoms and molecules using optical excitation. Measurements of lifetimes have improved as optical sources of radiation have evolved. Here, we present a sampling of different methods that have been used to obtain various lifetimes.

Two kinds of optical excitation (pulsed excitation and phase-shift methods) have been used for measuring excited-state lifetimes. In pulsed excitation method, atoms and molecules are excited by an pulsed of optical radiation and the population of excited states are monitored by measuring the resulting time-dependent fluorescence or absorption. In the phase-shift (sinusoidally excitation) methods, the atoms and molecules are excited by radiation with an intensity that oscillates at a frequency ν and the lifetime is determined by measuring the phase difference between the excitation and fluorescence or absorption decay waveform.

Over the last fifty years, pulsed sources of radiation have evolved from mechanically chopped lamps [5] to flashlamps [68, 38] to pulsed laser sources [48]. At the same time, a variety of optical modulation techniques including mechanical modulators, rotating diffraction gratings [43], Kerr and Pockets cells have been developed [51]. These techniques increased the time resolution of lifetime measurements from tens of microseconds to fractions of a picosecond. [21, 62].

One of the earliest reported direct measurement of lifetime $0.98 \times 10^{-7} S$ for the 6^3P_1

state of mercury by Wien in 1919 [3, 71]. Here, a beam of ions are accelerated using an electric field. As ions recombine and emit light, the intensity along the beam show decay of the number of resonance atoms. From this decay curve the lifetime was obtained.

Other groups took advantage of the Kerr effect in early 1920's [62]. The Kerr effect was discovered by Scottish physicist John Kerr in 1875. He noted that the index of refraction of a material is changed with the application of an electric field. Using this principle, a Kerr cell shutter was developed and with this method the lifetime of Na was reported by monitoring the phase-delay in the observed fluorescence where the lifetime 1.5×10^{-8} s of both D lines [3, 28] at a temperature between 190^oC and 200^oC. Repetition of this experiment, with the same apparatus by Duschinsky in 1932 was in excellent agreement [3, 15] .

Resolution of tens of microseconds was achieved using mechanical systems. One such example is the 1969 work of Schwartz and Johnston in which they report a measurement of lifetimes in NO_2 and show a steady increase in lifetime from 60 μs to 90 μs over the range of excitation wavelengths 398-600 nm [65]. Here a xenon arc lamp chopped by a mechanical wheel driven at 60 Hz with 60 blades was used for excitation.

Sub-microsecond lifetime measurements became available with the advent of powerful flashlamps. Here, flashlamps were used for excitation after that the fluorescence of excited-levels were observed at a right angle using photomultiplier tubes. In an early study of this type Spears and Rice reported the lifetime measurement of vibrationally excited benzene to be 82 ns [68].

The introduction of pulsed lasers had a dramatic impact on lifetime measurements. These lasers allowed shorter (ns) pulse of laser radiation with far better spectral resolution and intensity than possible with flashlamp sources. A typical example is the 1974 work of

Brus and McDonald reporting the measurement of independent rovibronic states dependent of SO_2 by using a Q-switch Nd:YAG [40]. This degree of state selection is typical of a laser-based measurement and beyond the capabilities of a flashlamp-based experiment. By the end of the 1970's laser-based measurements had all but replaced flashlamp based experiments.

In recent years, laser pulses have decreased to the subfemtosecond range. Measurements of lifetimes in this new regime become complicated by the fact that the response of light-detecting systems (such as diodes and photomultiplier tubes) are typically limited to about 0.1 ns. This short coming led to the autocorrelation methods described in the next sections.

3.1.4 Intensity Autocorrelation

The intensity autocorrelation method is the most common technique used to measure the time profile of an ultrashort laser pulse. This technique was developed in early 1960s [61] . The intensity autocorrelation usually involves splitting a laser pulse into two beams and delaying one with respect to the other (see Figure 3.3). After this delay, the two laser beams are recombined and allowed to passed through a rapidly responding nonlinear crystal.

This second-harmonic-generation(SHG) crystal converts the input radiation at a frequency ω to a signal radiation at a frequency 2ω. This SHG signal has its maximum when the two input pulses overlap perfectly in time. The SHG intensity as a function of the optical delay gives an autocorrelation measurement. This technique allows one to gain sensitivity to the time-dependent intensity I(t) of the radiation. Specifically, the delay dependent

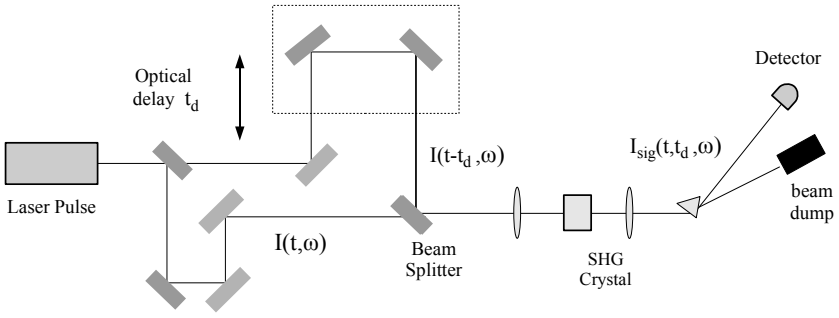

Figure 3.3: Typical experimental setup for the intensity autocorrelation.

intensity I(t,t_d) determined by the autocorrelation function.

$$A(t_d) = \int_{-\infty}^{\infty} I(t)I(t - t_d)dt. \tag{3.1}$$

Here $t_d = \frac{d}{c}$ is the delay.

The autocorrelation measurement relies on a crystal response time that is much faster than the duration of the pulse of laser radiation. When the crystal is replaced by a time-sensitive system, such as a decaying molecule, then the technique will measure the properties of the system rather than that of the radiation [2]. This situation is the case for our measurement of the lifetime of PbF molecules. In the next section, we outline the experimental details for lifetime measurements of D state of the PbF molecules. Results and conclusions are given in the following section.

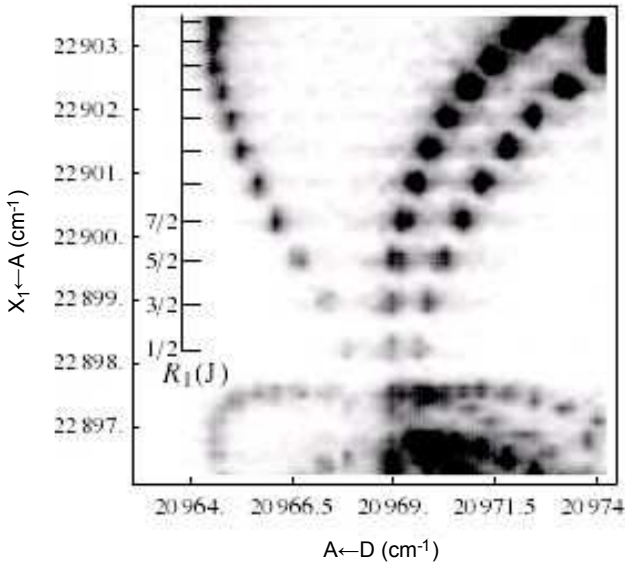

Figure 3.4: 1+1+1 REMPI ionization of PbF and the spectra gives the ion signal of one A$\leftarrow$ X_1 transition and other A$\leftarrow$D transition.

3.2 Experiment

3.2.1 Laser Radiation and Ionization Scheme

Production of PbF molecules has been explained in detail in the previous chapter and elsewhere [7, 57]. In brief, PbF molecules are created from the reaction of molten Pb with the MgF_2 surface of a nozzle and enter into a source chamber. Then this beam passes through a skimmer and enters a differentially pumped chamber. The beam then intersects with cylindrically focused laser radiation which ionizes PbF molecules. These ions are then accelerated by an uniform electric field to a micro channel plate detector and detected with sufficient mass resolution to separate the $^{206}Pb^{19}F$, $^{207}Pb^{19}F$ and $^{208}Pb^{19}F$ isotopomers [7, 57].

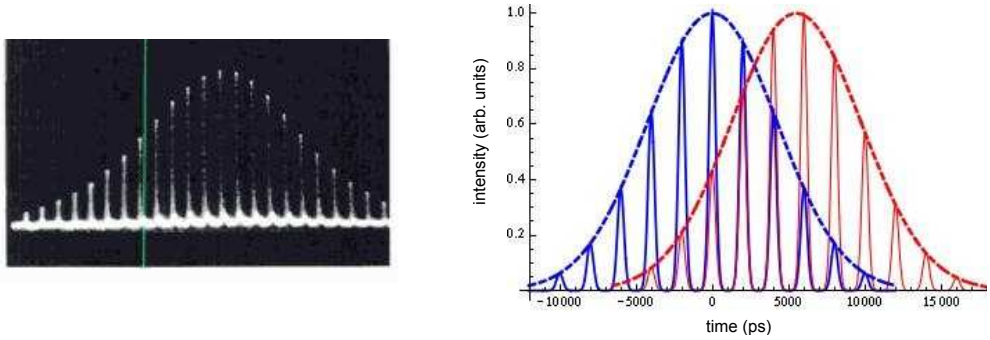

(a) (b)

Figure 3.5: (a) Temporal structure of unseeded Nd:YAG laser radiation (taken from a Spectra Physics laser manual) and (b) a simple illustration of picosecond pulsed correlation inside the nanosecond envelope.

The three-photon ionization scheme of Figure 3.1 is used to ionize PbF. Specifically, molecules are ionized by driving A $^2\Sigma^+_{1/2}(v = 1) \leftarrow$ X$_1$ $^2\Pi_{1/2}(v = 0)$ transition at 436.6-nm (vacuum) and the D$(v = 0) \leftarrow$ A $^2\Sigma^+_{1/2}(v = 1)$ transition at 476.6-nm laser radiation. Finally, the D-state molecules are ionized by driving the PbF$^+ \leftarrow$ D$(v = 0)$ transition with 532-nm laser radiation. When narrow bandwidth laser radiation is used to drive the first two steps, the 1+1+1 REMPI spectrum shown in Figure 3.4 and reference [57] is obtained. For this work, the X-A laser is tuned to an R branch pile up and the A-D transition is excited using broad bandwidth laser radiation (see section 2.1) so that the $19/2 <= J <= 27/2$ transitions are simultaneously excited.

3.2.2 Measurement of the Lifetime of the D state of PbF

It may at first seem that the 10-ns pulses of laser radiation created by our Nd:YAG pumped dye laser system could not be used to create time-dependent measurements of a

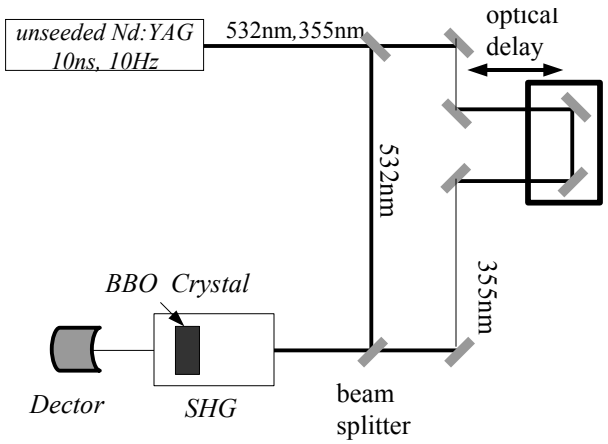

Figure 3.6: Optical bench setup to make correlation spectra of 355- and 532-nm laser radiation.

sub-nanosecond lifetime. However, the Nd:YAG pump laser is unseeded. As a result, it has temporal structure on the picosecond time scale. Specifically, laser radiation from our Nd:YAG laser is emitted in a series of picosecond pulses separated by the round-trip cavity length and occurring with a 10-ns intensity envelope (Figure 3.5).

This structure can be observed in the autocorrelation measurement shown in Figure 3.6. Here the second harmonic 532-nm and third harmonic 355-nm laser radiation is combined in a β-barium borate (BBO) crystal to create 212.8-nm light. By varying an optical delay between the 355-nm and 532-nm radiation, the intensity correlation between the two laser beam obtained and reveals a coherent spike of width of 50 ps. Figure 3.7. As expected a second pulse was observed at an optical delay equivalent to the round-trip distance of the Nd:YAG laser cavity.

To measure the D-state lifetime, we need to create a situation for which a correlation exists between the output of 476-nm tunable dye laser radiation driving the D $\leftarrow$ A transition

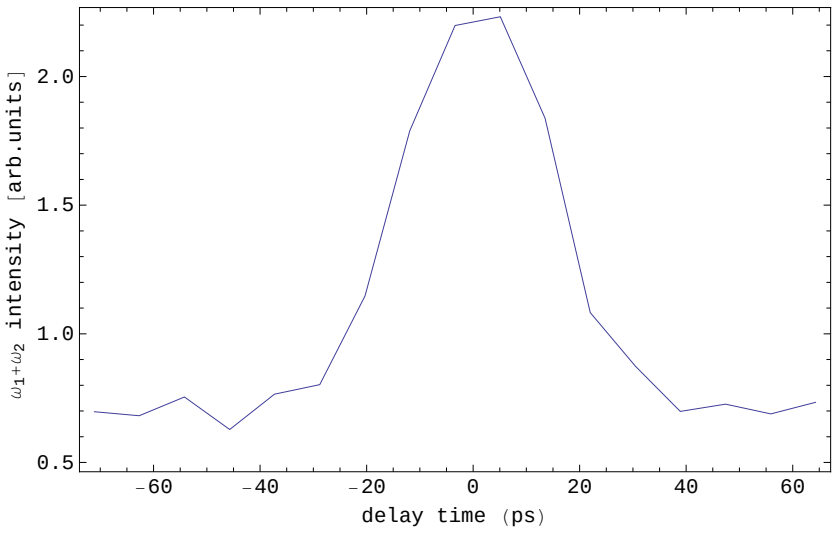

Figure 3.7: Correlation spectra giving the time-domain temporal overlap of the 355- and 532-nm laser radiation.

and the 532-nm Nd:YAG laser radiation ionizing the D-state. To create this correlation, we first attempted to generate the 476-nm laser radiation by pumping our Lambda Physik Scanmate IIe dye laser with 355-nm laser radiation as its fundamental output. However, we discovered that laser radiation produced in this way was not correlated to the 532-nm laser radiation on a picosecond time scale. Apparently, the output of a Coumarin dye laser does not follow the time dependence of its 355-nm pump.

Achievement of a correlation between the 476.6-nm and 532-nm laser radiation required a substantial reworking of our optical bench Figure 3.8. Here the 532-nm of the Nd:YAG laser is split into two beams and the first is used to pump the infrared dye LDS-867 to produce 863-nm laser radiation. The fundamental of the Nd:YAG laser (at 1064-nm) is

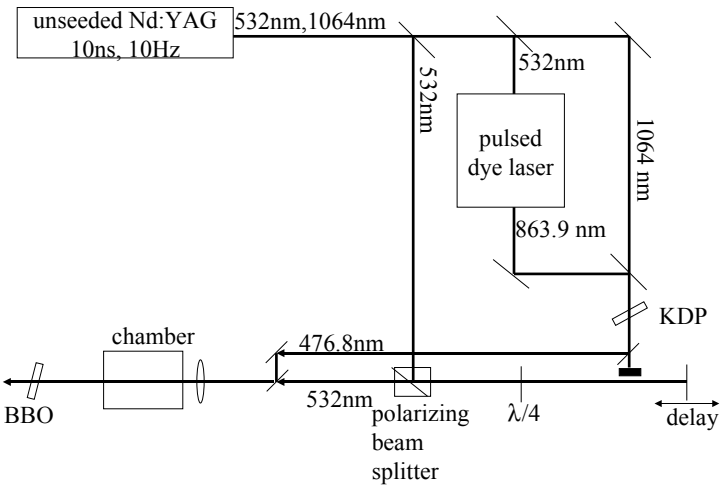

Figure 3.8: Optical bench setup to make correlation spectra of 476- and 532-nm laser radiation.

then mixed with the 863-nm laser radiation to create 476.6-nm laser radiation. By creating 476.-nm laser radiation in this way, the 476-nm radiation follows the temporal structure of the Nd:YAG laser. This is observed by mixing the 532-nm output of the Nd:YAG laser with the 476.6-nm laser radiation in a BBO crystal to create 251-nm laser radiation. The temporal correlation is obtained by optically delaying the 532-nm laser radiation with respect to 476.6-nm radiation and monitoring the intensity of the 251-nm signal. This measurement reveals a coherent spike of width 60 ps shown in Figure 3.9.

To obtain the lifetime of the D-state of the PbF molecule, the measurement of Figure 3.9 is repeated, but with the harmonic generation crystal replaced with the ionization process. Specifically, the BBO crystal is removed and the 476.6-nm and 532-nm laser radiation is instead focused (along with the 436-nm laser radiation driving the $A \leftarrow X_1$ transition) onto the molecular beam. The PbF (isotope averaged) ionization signal is then monitored as a

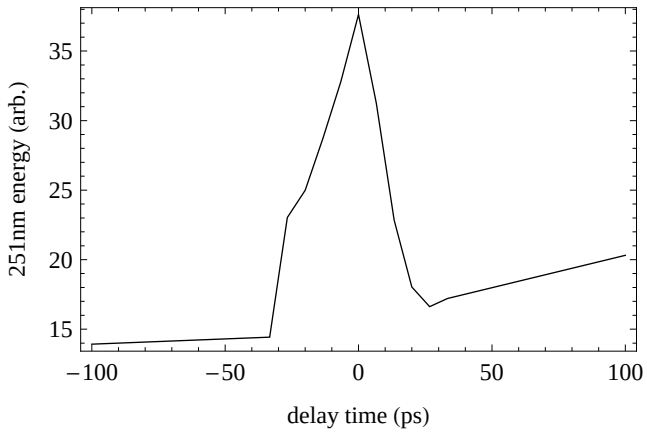

Figure 3.9: Correlation spectra giving the time-domain temporal overlap of the 476- and 532-nm laser radiation.

function of an optical delay between the 476.6-nm and 532-nm laser radiation. The resulting optical-delay-time-dependent signal is shown in Figure 3.9.

In our measurement of the D state lifetime , the A $\leftarrow$ X_1 laser radiation is tuned to the 0-1 band head of A $\leftarrow$ X_1 transition 436.6 nm (vacuum) to excite approximately five rotational levels centered around $J = 23/2$.

3.3 Data Analysis

We created a simple mathematical model to find the lifetime of the D state by treating the ionization scheme of the PbF molecule as a two state system containing the A-state and the D-state see Figure 3.2(a). Here, the lifetime of the A state ($\tau > 1\mu s$ [33]) is much larger than the expected D-state lifetime. Therefore, the A-state essentially never decays and it can be treated as if it were the initial state for our model.

In this model, we assumed PbF^+ $\leftarrow$ D $\leftarrow$ A process for our kinetic model as shown in

Figure 3.2(a) and the model calculate the population of ionization signal as a function of lifetime of D state ($k_d = 1/\tau_d$) and optical delays between the 476-nm and 532-nm laser radiation. After that, we fit this model ionization signal to our measurement of exponential decay as delay the 532-nm respect to 476-nm laser radiation.

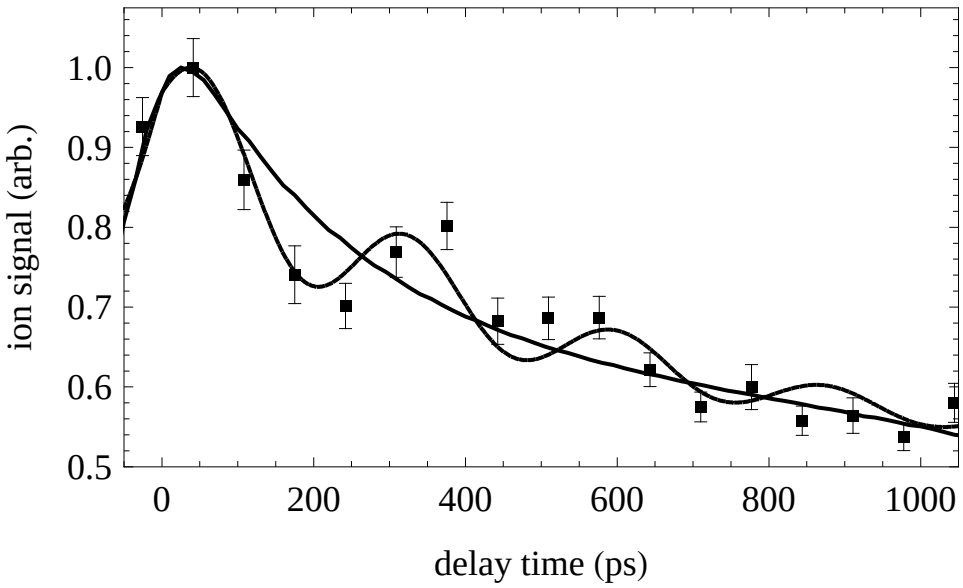

Figure 3.10: Correlation spectra giving the time-dependent decay of the D-state.

The resulting simulated time-dependent ionization signal is shown by the solid line in Figure 3.10. The result of our lifetime measurement shows an oscillatory structure enveloped by exponential decay. We interpret this oscillatory structure to be caused by interference between the many rotational levels of the initially excited state and the exponential decay is due to the lifetime of D state. From this, we determine the lifetime of D state is 250± 150 ps. The large error is due to our inability to model the oscillatory component of the decaying ionization signal.

3.4 Results and Conclusion

We have determined the lifetime (subnanosecond) of the D(v=0) state of the PbF molecules to be 250± 150 ps using an unseeded 10-ns Nd:YAG laser system to perform an intensity correlation measurement. This lifetime can also be estimated from the reciprocal of the $0.33 - cm^{-1}$ linewidth of the D ← A transitions of the spectra shown in Figure 3.4. This reciprocal gives a lifetime of 100 ps, in reasonable agreement with our time-domain measurement. We caution, however, that the linewidth measurement is only a lower limit and its agreement with our time-dependent measurement is somewhat fortuitous. This lifetime measurement allowed us to conclude that a pseudo-continuous picosecond laser system is the appropriate choice for ultra-sensitive detection of the PbF molecule.

This work was inspired by a desire to measure a lifetime that was too long to be resolved in a linewidth measurement yet to short to be measured directly with our 10-Hz, 10-ns Nd:YAG-pumped dye laser system. The technique we developed to obtain 100-ps-sensitivity with a 10-ns-pulsed laser may prove useful to others who have access to similar systems and need to measure sub-nanosecond dynamics.

Chapter 4

Development of Pseudo Continuous Resonance Enhanced Multiphoton Ionization (pc-REMPI): Application to the measurements of the hyperfine levels of PbF

4.1 Introduction

In this chapter, we demonstrate a method of multi-photon ionization that provides for sensitive detection of PbF with ultra high resolution (90MHz). To obtained this resolution, we combined narrow bandwidth diode laser radiation with a pseudo-continuous laser radiation produced from an optical parametric oscillator. The diode laser radiation is used to drive the $A(v' = 1) \leftarrow X_1(v = 0)$ transition and achieve the ultra high resolution. The pseudo-continuous laser radiation drove the ionization process ($PbF^+ \leftarrow D(v'' = 0) \leftarrow A(v' = 1)$) allowing us to achieve ultra high sensitivity. The result of these improvements was a factor of approximately 30 times better resolution and 100 times greater sensitivity over our implementation of conventional REMPI detection. We refer to this improved detection technique as *Pseudo-Continuous Resonance Enhanced Multiphoton Ionization* or pc-REMPI.

The following description of pc-REMPI and its application to the determination of hyperfine interaction constants that model the interaction of the ^{19}F nucleus with the unpaired electron spin in A and X_1 states is as appears (with minor modification) in a recent publication [58].

Resonance-enhanced multi-photon ionization (REMPI) spectroscopy became a useful tool for molecular spectroscopy with the spread of tunable ns dye lasers in the 1970s [13, 11, 54]. Numerous subsequent extensions and applications of the basic technique have exploited different combinations of ion counting, photoelectrons detection, mass resolution through time of flight techniques, and recoil velocity measurements. In the present work, we describe a new variation of the technique that provides a sensitive method for the detection of the absorption of a high resolution, but low power, continuous wave laser and use it to measure hyperfine resolved spectra of ^{208}Pb^{19}F.

Typically REMPI is carried out with pulsed laser systems running at a repetition rate of $10 - 5000$ Hz. Ions created from each pulse of laser radiation are collected onto a micro-channel plate detector. Mass selection is achieved by measuring the time between the arrival of the pulse of laser radiation and the arrival of the ion at the detector. This pulsed-detection scenario often is ideally suited to an experimental measurement. For example, in the study of the dynamics of a photo-dissociation or photo-initiated reaction, the pulse of detection radiation must be timed precisely with respect to the pulse of radiation used to dissociate a molecule. For this case, the experiment is not limited by the repetition rate of the detection laser radiation, but rather by the time it takes to replenish a fresh sample of gas into an interaction volume.

For other experiments, the pulsed detection scenario is severely limiting. An important example is precision beam spectroscopy that requires the resolution of a continuous wave (cw) laser. For a pulsed ionization-detected cw absorption measurement, two factors can limit the ionization signal levels. A purely geometrical upper bound on the duty cycle will be given by the sample transit time across the pulsed beam focal volume, divided by the pulse repetition period. With sufficient power in the pulsed laser, saturation conditions can be achieved in relatively large focal volumes. In this case the effective duty cycle may instead be limited by a second factor: the ratio of the lifetime of the excited state produced by the cw laser relative to the repetition rate of the pulsed laser. This ratio varies widely from experiment to experiment. For excitation of the $A \leftarrow X_1$ transition of PbF with our 10-Hz pulsed laser system, the 5- μs lifetime of the A state [66] implies an effective ionization duty cycle of $1 : 2 \times 10^4$. In addition to the obvious drawbacks of such a small duty cycle, experiments driven by short pulses of radiation occurring at low repetition rates may also suffer from large 1/f noise.

Here we report a technique that marries the advantages of REMPI with the narrow resolution of cw excitation. Specifically, we combine narrow bandwidth diode laser radiation with pseudo-continuous laser radiation to enable a *pseudo continuous resonance enhanced ionization scheme* which we refer to as pc-REMPI. We apply this pc-REMPI technique to obtain a high resolution spectra of the A $^2\Sigma_{1/2}(v' = 1) \leftarrow$ X$_1$ $^2\Pi_{1/2}(v = 0)$ transition in PbF. This $1-0$ band spectra allows us to determine the hyperfine constants that describe the interaction of the ^{19}F nucleus with the unpaired electron spin in both the A and X$_1$ states. Our motivation to develop this technique is to both obtain these spectroscopic constants and to create an ultra-sensitive scheme for the detection of PbF. The PbF molecule may

play an important role in the measurement of the electron's electric dipole moment (e-EDM) [7, 8, 47, 50, 57].

The next section describes the experimental technique. Section 4.3 gives the data analysis in terms of a spin-rotational Hamiltonian. Results are summarized in section 4.4

4.2 Experimental

The experiment is shown in schematically in Figure 4.1. Ionization occurs via the double resonant ionization process $PbF^+ \leftarrow D(v'' = 0) \leftarrow A(v' = 1) \leftarrow X_1(v = 0)$ [57]. The $A \leftarrow X_1$ transition is driven with 6 mW of 436-nm radiation produced by an optically isolated (Optics for Research IO-5-λ-LP, Figure 4.1-1-) diode laser (Toptica DL-100,Figure 4.1-2-). The $PbF^+ \leftarrow D(v'' = 0) \leftarrow A(v' = 1)$ ionization process is driven by 6-ps pulses of 476 nm radiation that occur at a repetition rate of 76 MHz. The 6 ps pulse width is chosen to be less than the measured lifetime of the D state [57]. The average power of this 476 nm laser radiation is typically 700 mW. This source of radiation is created in the following manner: The 532 nm second harmonic output of a 6 ps, 76 MHz, mode-locked Neodymium doped Yttrium Vanadate (Nd:YVO_4) laser (HighQLaser, picoTrain Figure 4.1-7-) is used to pump an optical parametric oscillator (OPO, Angewandte Physik und Elektronik Levante Emerald,Figure 4.1-6-). The output optics of the Nd:YVO_4 laser are modified in order to gain access to the residual 1064 nm laser radiation. The temperature of the second harmonic generation crystal internal to the Nd:YVO_4 laser system is adjusted to produce 5.5 watts of 532-nm laser radiation (the maximum that can be safely used to pump the OPO) and 2.0 watts of residual 1064-nm laser radiation. The OPO produces approximately

1.5 watts of 864 nm laser radiation which is combined in a Lithium Triborate crystal (LBO, Red Optronics,Figure 4.1-8-) with the residual 1064 nm laser radiation in order to create the required 476 nm laser radiation by type II sum-frequency generation.

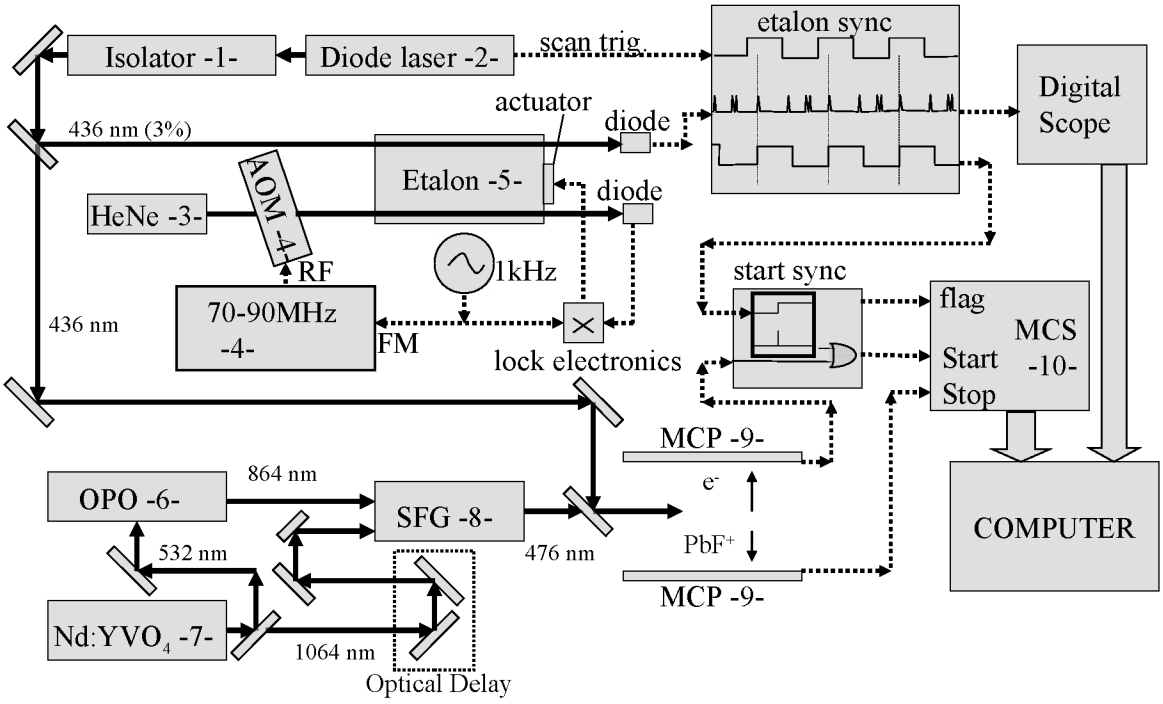

Figure 4.1: Experimental schematic for determination of hyperfine interaction constants of $^{208}Pb^{19}F$.

An effusive beam of PbF molecules is created by heating molten lead to 1000°C (typical) in a MgF_2 nozzle[7, 57]. Molecules created in this way enter into a differentially-pumped detection region through a 1.0 mm skimmer. Molecules that travel into the region of focused laser radiation are state-selectively ionized, creating a e^-/PbF^+ pair. The electrons created

in this way are accelerated by a uniform electric field to a micro-channel plate detector (Figure 4.1-9-), and into a timing amplifier (Ortec model 9327) which creates a *start* pulse. The ions are accelerated in the opposite direction to a second micro-channel plate detector, creating a *stop* pulse.

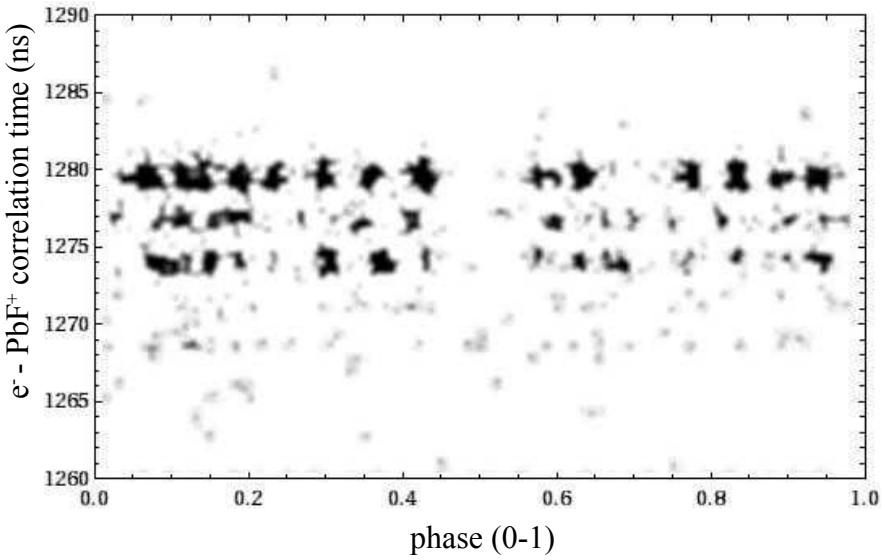

Figure 4.2: Row data of the Q_{fe} branch pileup of the $A(v' = 1) \leftarrow X_1(v = 0)$ transition in $^{208}Pb^{19}F$ Also visible at shorter $e^- - PbF^+$ correlation times are $A \leftarrow X_1$ transitions in $^{207}Pb^{19}F$ and $^{206}Pb^{19}F$. Conversion from phase to frequency is achieved by calibration to a cavity stabilized etalon, as described in the text.

The start and stop pulses are fed into a multi-channel scaler (Ortec model 9353, Figure 4.1-10-) that logs the events as a function of both the start-stop delay (giving mass resolution) and the time of the start pulse with respect to an internal clock. This internal clock is synchronized to the diode laser frequency sweep by sending synchronization (sync)

pulses to the multi-channel scalar. These sync pulses coincide with the transmission of light through a 1 GHz FSR etalon (Toptica, FPI 100, Figure 4.1-5-). This etalon is stabilized with a Zeeman stabilized HeNe laser (MicroG LeCoste, ML-1, Figure 1 -3-) that is modulated by an Acoustic-Optical device (Newport Electro Optics Systems, N21080-1SAS, Figure 4.1-4-). A computer is used to accumulate these events as a function of relative frequency and time of flight.

Typical raw data is shown in Figure 4.2 These data show the Q_{fe}-branch pile up of the $A(v' = 1, J' = J, f) \leftarrow X_1(v = 0, J, e)$ transition. The x-axis of this plot gives the phase of the start pulse timing with respect to the diode laser scan whereas the y-axis gives the time of flight (start-stop delay). The spectral plot of Figure 4.3 is obtained by integrating over a start-stop delay window that isolates the $^{208}Pb^{19}$ F signal and converting the start-stop phase to a frequency shift. By patching together many such scans, we are able to create the spectra of Figure 4.3 . The line width of the spectra shown is 90 MHz. As can be seen in Figure 4.4 this resolution is sufficient to isolate the e-EDM sensitive $Q_{fe,0,1}(1/2)$ transitions. We estimate that the absolute accuracy of this spectra is about 1 GHz, as determined by both the limited accuracy of our wave meter (Burleigh WA-1000) and our patching technique. The precision with which we can measure resolved line splittings is about 10 MHz and is limited by nonlinearity in the scanning mode of the DL100 diode laser.

We note that this scan shows no sensitivity to the high J lines of the R_{ff} branch. The absence of these lines does not reflect the rotational temperature of the beam (which we measure in a separate work to be 1000^oC [57].) Instead, the lines do not appear because the wavelength of the ps laser system is fixed during the scan of Figure 4.3. By adjusting

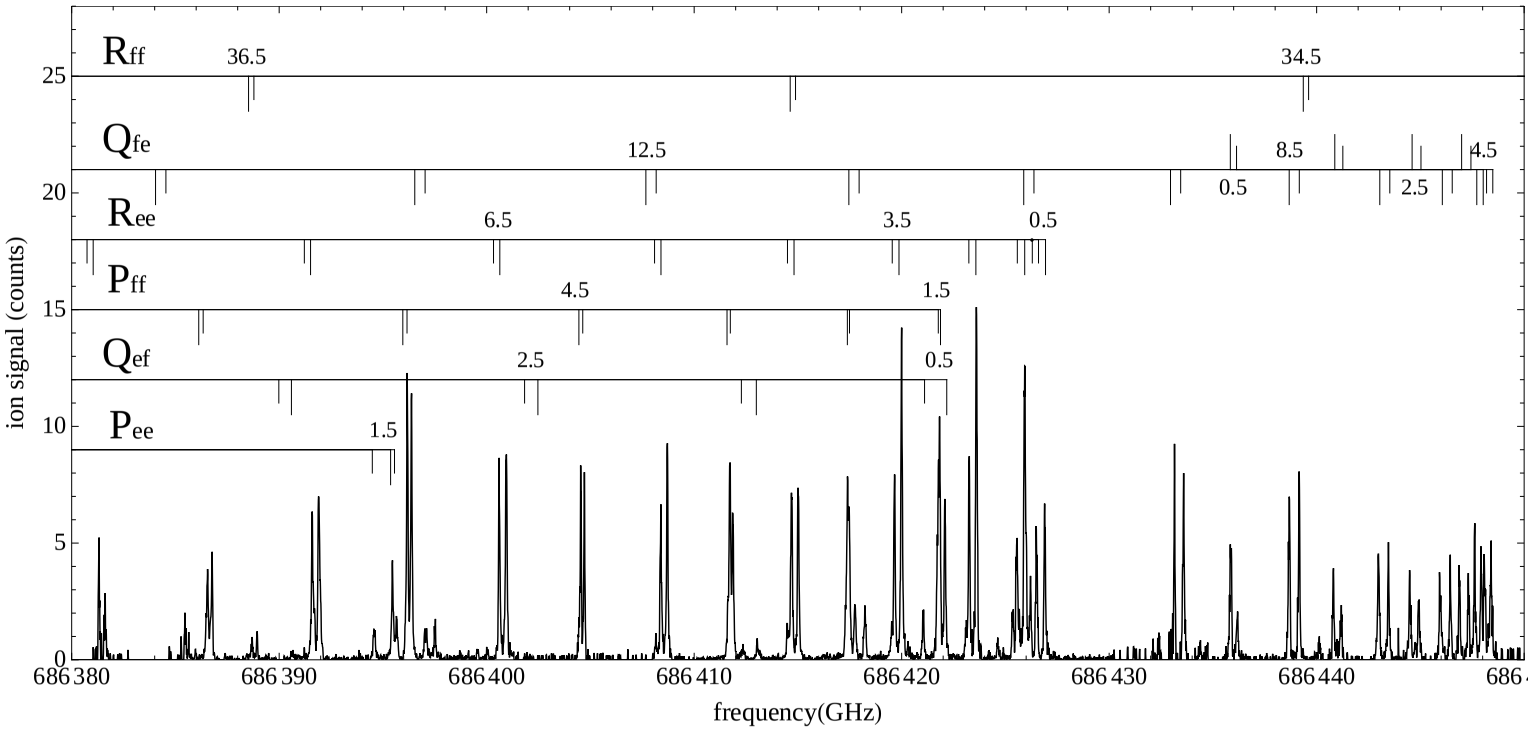

Figure 4.3: Observed spectrum of the $A(V' = 1) \leftarrow X_1(v'' = 0)$ band of $^{208}Pb^{19}F$. In the line assignments, short markers indicate $F = J - 1/2$ transitions whereas long markers indicate $F = J + 1/2$ transitions.

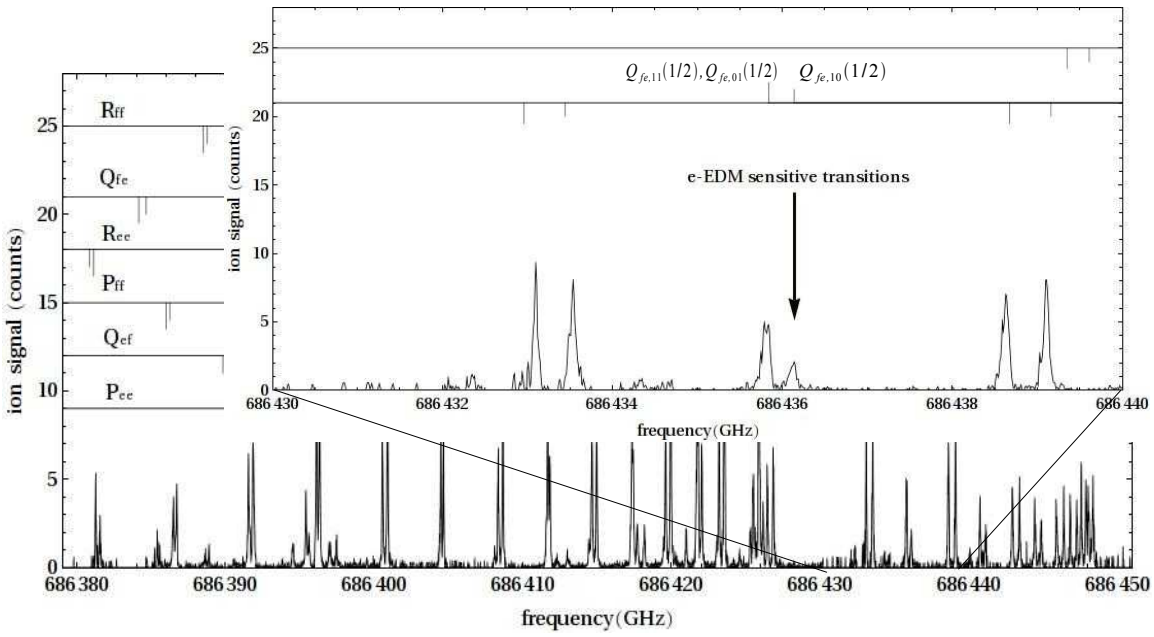

Figure 4.4: Isolation of an e-EDM sensitive transitions of $^{208}Pb^{19}F$.

the wavelength of the pseudo-continuous laser radiation driving the D←A transition, the $R_{ff}(69/2)$, $R_{ff}(71/2)$, and $R_{ff}(73/2)$ can be made to dominate the spectra. We also note that we observe significant line narrowing when Ne is used as a buffer gas instead of He. This suggests that the molecular beam undergoes significant translational cooling, but little or no rotational cooling.

Typical on-resonance e^-–PbF^+ event rates are 10 to 100 Hz. The introduction of this paper contrasts pc-REMPI with a measurement that employs a cw laser to excite PbF molecules to the A state followed by ionization by radiation from a 10-Hz pulsed laser system (cw+REMPI). It is difficult to access the improvement of pc-REMPI over this cw+REMPI scheme, as attempts to observe PbF^+ by this second method were unsuccessful.

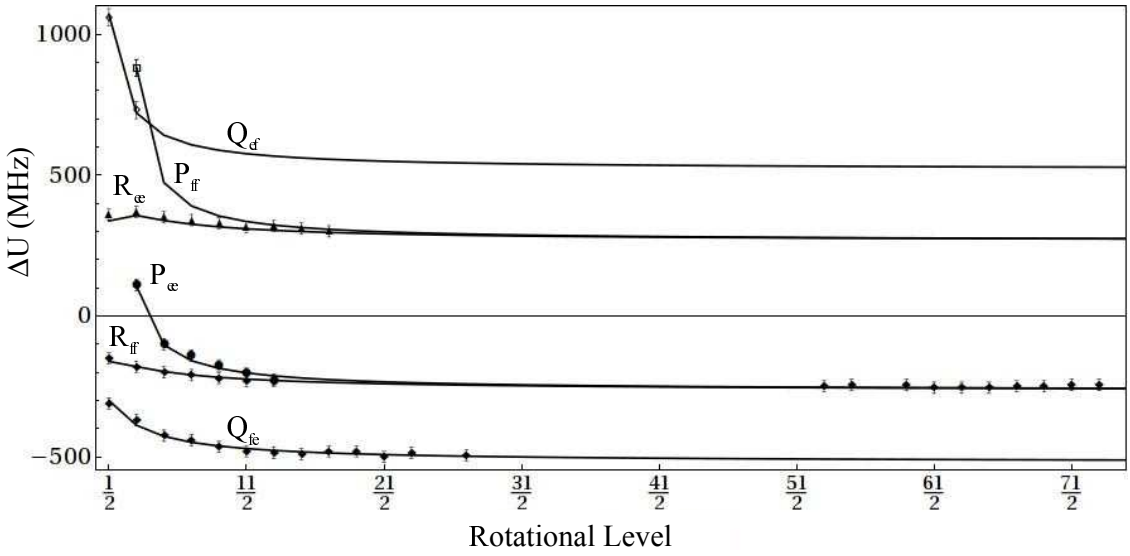

Figure 4.5: .The J-dependent splitting between the $\mathrm{A}(v' = 1, j'F' = J' + \frac{1}{2} \leftarrow \mathrm{X}_1(v = 0, J, F = J + \frac{1}{2}$ and $\mathrm{A}(v' = 1, j'F' = J' - \frac{1}{2} \leftarrow \mathrm{X}_1(v = 0, J, F = J - \frac{1}{2}$ transitions. The best fit prediction of Eq 4.9 (solid lines) is compared to experiment (markers).

The improvement is expected to be less dramatic than the factor of 2×10^4 inferred from the effective duty cycle of the cw+REMPI measurement. The large peak powers of our pulsed laser system allow for a much greater depth of focus and hence a larger probe volume. With this consideration, we estimate an improvement in sensitivity of a factor of 10^3. This leads to an expected collection rate (0.01 Hz to 0.1 Hz) that is consistent with our failure to observe PbF^+ generated from the cw+REMPI process.

4.3 Determination of the Hyperfine Constants of $^{208}Pb^{19}F$

The rotational spectra of levels of the X_1 and A states of $^{208}Pb^{19}F$ have been well characterized elsewhere [14, 33, 44, 63, 64, 67, 73]. Here we are chiefly concerned with interpreting the hyperfine splitting of each of the rotational transitions we observe. The hyperfine structure of the energy levels of an $\Omega = 1/2$ molecule are often described in terms of the Frosch and Foley Hamiltonian [29, 31, 35, 59]:

$$H_{hfs} = aI' \cdot L + (b+c)I'_z S_z + \frac{b}{2}(I'_+ S_- + I'_- S_+) + \frac{d}{2}e^{2i\phi} I'_- S_- + \frac{d}{2}e^{-2i\phi} I'_+ S_+. \tag{4.1}$$

If we assume that the valence electron has a wave function of the form

$$\psi_{\pm 1/2} = \sum_{\ell=0}^{\infty} [c_\ell^0 |\ell, 0\rangle| \pm \frac{1}{2}\rangle + c_\ell^1 |\ell, 1\rangle| \mp \frac{1}{2}\rangle] \tag{4.2}$$

then the spectra will be sensitive to the following linear combinations of the Frosch and Foley parameters:

$$A_{||} = \sum_{\ell=0}^{\infty} \left(|c_\ell^0|^2 (b+c) + |c_\ell^1|^2 \left(2a - (b+c)\right)\right) \tag{4.3}$$

$$A_{\perp} = \sum_{\ell=0}^{\infty} \left(-a\sqrt{\ell(\ell+1)} \left(c_\ell^{1*} c_\ell^0 + c_\ell^{0*} c_\ell^1 \right) - b|c_\ell^0|^2 + d|c_\ell^1|^2 \right). \tag{4.4}$$

For a σ orbital, $A_{||} = b + c$ and $A_\perp = -b$ whereas for a π orbital $A_{||} = 2a - b - c$ and $A_\perp = d$. These hyperfine parameters are the fine-structure parameters that describe the hyperfine interaction in terms of an effective spin-rotational Hamiltonian [39, 45] with

$$H_{hfs} = I' \cdot \hat{A} \cdot S' \tag{4.5}$$

$$= \sum_t (-1)^t A_t I'^1_t S'^1_{-t}. \tag{4.6}$$

Here I' acts on the molecular-frame nuclear spin and S' is the pseudo-spin operator that acts on Ω. The resulting spin-rotational energy is given elsewhere [8, 46] and, in the reference[58],

shown to have the following form:

$$U_{sr} = U_{rot} + U_{HF}$$

$$U_{rot} = BJ(J+1) - D\left[J(J+1)\right]^2 - q\chi\,\frac{p}{2}(J+\frac{1}{2}) \tag{4.7}$$

$$U_{HF} = \frac{\chi A_\perp}{4} - \frac{q(A_{||} - \chi A_\perp)}{4(2F+1)} + q\frac{\Delta_{F,\chi}}{2} G\left[\frac{A_{||} - \chi A_\perp}{\Delta_{F,\chi}}\sqrt{\frac{F(F+1)}{(2F+1)^2}}\right] \tag{4.8}$$

$$\approx \frac{\chi A_\perp}{4} - \frac{q(A_{||} - \chi A_\perp)}{4(2F+1)}. \tag{4.9}$$

where $p_s = \pm 1$ gives the parity with respect to all coordinates except nuclear spin, $\chi = \pm 1 = (-1)^F p_s$, $q = \pm 1 = 2(J-F)$, and

$$G[x] = \sqrt{1+x^2} - 1 \tag{4.10}$$

$$\Delta_{F,\chi} = (2F+1)\left(B - \frac{p}{2}\chi - \frac{1}{2}D(2F+1)^2 - \frac{A_{||} - \chi A_\perp}{2(2F+1)^2}\right). \tag{4.11}$$

The approximation of Eq 4.9 is valid when $\Delta_{F,\chi} >> A_{||}, A_\perp$. For our case, the term involving $\Delta_{F,\chi}$ causes a correction to the ground $J = 1/2$ state energies of about 4 MHz, with the correction rapidly decreasing with increasing J.

We label each allowed $\mathrm{A}(J', p_s') \leftarrow \mathrm{X}_1(J, p_s)$ transition by $\mathrm{R_{ee}(J)}$, $\mathrm{R_{ff}(J)}$, $\mathrm{P_{ee}(J)}$, $\mathrm{P_{ff}(J)}$, $\mathrm{Q_{ef}(J)}$, or $\mathrm{Q_{fe}}(J)$. Here R, P and Q indicate $J' = J+1, J-1$, and J respectively. The first subscript gives the sign of the product $q'\chi' = p_s'(-1)^{J'-1/2}$ for the A state, with e indicating $q'\chi' = 1$ and f indicating $q'\chi' = -1$. Similarly the second e/f subscript gives the $+/-$ sign of the product $q\chi$ for the X_1 state. For each transition with $J, J' > 3/2$, the $\Delta J = \Delta F$ transitions have a much greater dipole transition strength than the $\Delta J \neq \Delta F$ transitions and only one hyperfine splitting is observed. The $J >> \frac{1}{2}$ limiting form of this splitting, as determined by Eq 4.8, is given in Table 4.1.

Whereas $A_{\perp,X_1}$ and $A_{\perp,A}$ can be determined from high-J measurements, $A_{||,X_1}$ and

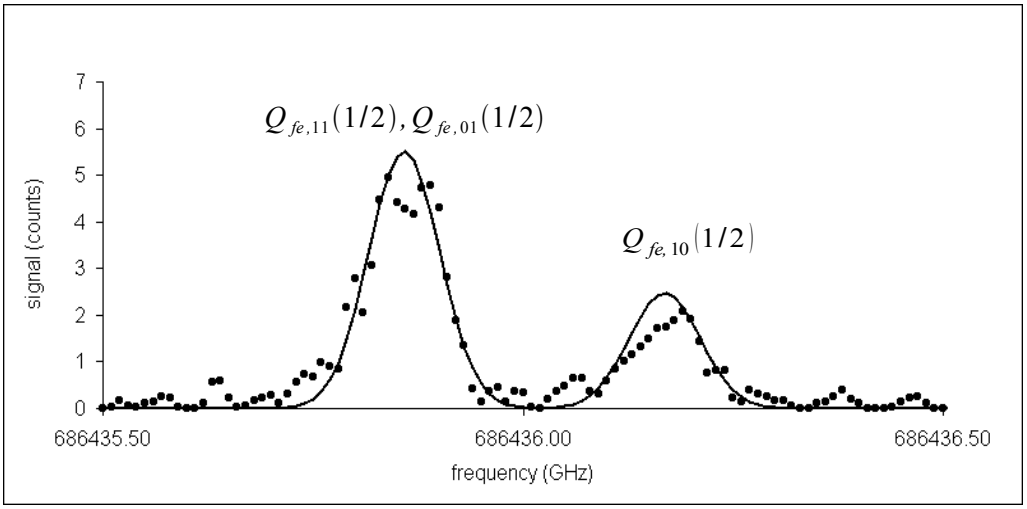

Figure 4.6: Experimental measurement of the $Q_{fe}(1/2)$ line profile (filled circles). The solid line gives the expected line shape given the energy distribution of Eq 4.8.

$A_{||,A}$ are most sensitive to the hyperfine structure of the $Q(\frac{1}{2})$, $R(\frac{1}{2})$ and $P(\frac{3}{2})$ transitions. For these transitions, the $\Delta J = \Delta F$ selection rule breaks, allowing us to observe splittings that depend individually on the energy levels of the X_1 and A states. For example the difference between the energy $Q_{ef,11}(\frac{1}{2})$ of the $A(J' = \frac{1}{2}, e, F' = 1) \leftarrow X_1(J = \frac{1}{2}, f, F = 1)$ transition and the energy $Q_{ef,01}(\frac{1}{2})$ of the $A(J' = \frac{1}{2}, e, F' = 0) \leftarrow X_1(J = \frac{1}{2}, f, F = 1)$ is a direct measurement of the $A(J' = \frac{1}{2}, e, F' = 0, 1)$ level splitting. This splitting is very nearly $(A_{||,A} - 2A_{\perp,A})/3$, as determined by Eq 4.9 and indicated in Table 4.1.

We note that, given our 90 MHz resolution, we are not able to resolve the $Q_{ef,11}(\frac{1}{2})$ and $Q_{ef,10}(\frac{1}{2})$ transitions, indicating that the $F_{X_1} = 0$ and $F_{X_1} = 1$ hyperfine levels of the ground Ω doublet state are very nearly degenerate. We are also unable to resolve the $Q_{fe,11}(\frac{1}{2})$ and $Q_{fe,01}(\frac{1}{2})$ transitions, indicating that the $F'_A = 0$ and $F'_A = 1$ levels of the upper Ω doublet

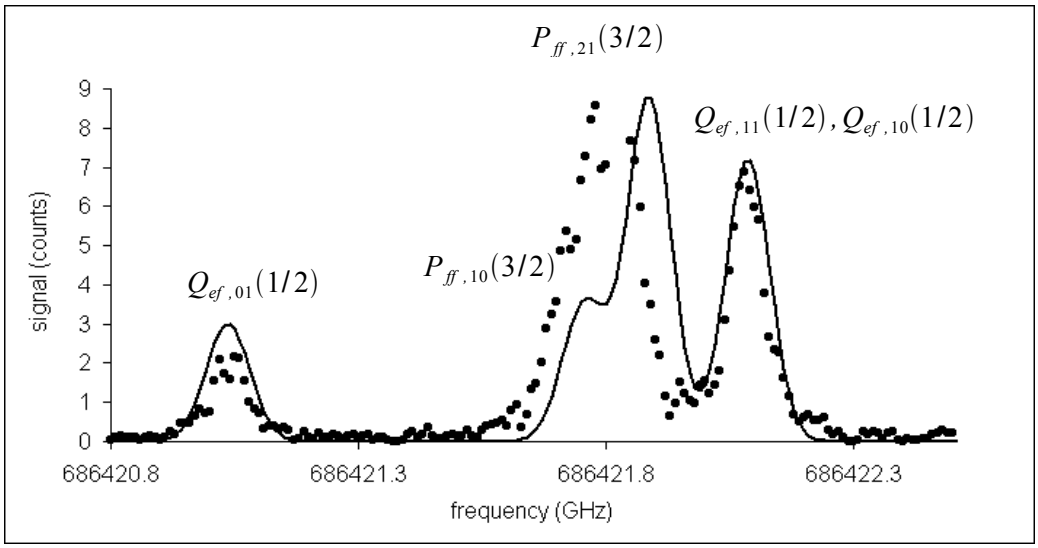

Figure 4.7: Experimental measurement of the $Q_{ef}(1/2)$ and $P_{ff}(3/2)$ line profiles (filled circles). The solid line gives the expected line shape given the energy distribution of Eq 4.8. The shift of the experimental $P_{ff}(3/2)$ line is due to the 1 kV/cm extraction field.

component of the $J' = 1/2$ level of the A state are very nearly degenerate.

To carry out our analysis, the parameters $p_{X_1} = -0.1382$ cm^{-1}, $B_{X_1} = 0.228027$ cm^{-1} and $D_{X_1} = 1.852 \times 10^{-7}$ cm^{-1} for the X_1 state are taken from Ziebarth et al [73] whereas the parameters $p_A = 0.6146$ cm^{-1}, $B_A = 0.20546$ cm^{-1}, $D_A = 2.21 \times 10^{-7}$ cm^{-1} for the A state are taken from Lumley et al[44].The four combinations of hyperfine parameters appearing in Table 1 are then varied to optimize agreement between experiment and the prediction of Eq 4.8 for (1) the hyperfine splittings of the R_{ee}, R_{ff} and Q_{fe} transitions as a function of J (Figure 4.5), (2) the line profile of the $Q_{fe}(1/2)$ hyperfine transitions (Figure 4.6), (3) the line profile of the $Q_{ef}(1/2)$ and $P_{ff}(3/2)$ transitions (Figure 4.7), and the line profiles of the $R_{ee}(1/2)$ and $P_{ff}(1/2)$ transitions (not shown).

Table 4.1: Combinations of hyperfine constants used to fit to experimental data

Parameter	fit*(MHz)	approximate relation to observation
$\frac{A_{\perp,A}-A_{\perp,X_1}}{2}$	-266 ± 7	$\Delta R_{ff}(J >> 1/2) = -\Delta R_{ee}(J >> 1/2)$
		$\Delta P_{ff}(J >> 3/2) = -\Delta P_{ee}(J >> 3/2)$
$\frac{A_{\perp,A}+A_{\perp,X_1}}{2}$	-520 ± 6	$\Delta Q_{fe}(J >> 1/2) = -\Delta Q_{ef}(J >> 1/2)$
$\frac{A_{\parallel,A}-2A_{\perp,A}}{3}$	1070 ± 10	$\Delta Q_{ef,11}(J = 1/2) - \Delta Q_{ef,01}(J = 1/2)$
		$= \Delta P_{ee,11}(J = 3/2) - \Delta P_{ee,01}(J = 3/2)$
$\frac{A_{\parallel,X_1}+2A_{\perp,X_1}}{3}$	-300 ± 20	$\Delta Q_{fe,11}(J = 1/2) - \Delta Q_{fe,10}(J = 1/2)$
		$= \Delta R_{ee,11}(J = 1/2) - \Delta R_{ee,01}(J = 1/2)$

The resulting values of hyperfine constants, as derived from the data in Table 4.1, are given in Table 4.2 :

Table 4.2: Measured hyperfine constants with errors that incorporate both statistical and an estimate of systematic contributions.

State	$A_\perp(MHz)$	$A_\parallel(MHz)$
X_1	-254 ± 11	392 ± 63
A	-785 ± 18	1640 ± 70

A systematic contribution to our error of 2% is due to alignment of the etalon used for frequency calibration and nonlinearity in the diode laser frequency ramp.

4.4 Summary and Conclusions

We have observed fully state-resolved spectroscopy of the $A(v' = 1) \leftarrow X_1(v = 0)$ transition in PbF using Pseudo Continuous Resonance Enhanced Multi-Photon Ionization (pc-REMPI). We have determined hyperfine constants for both the X_1 and A states of $^{208}Pb^{19}F$. This new pc-REMPI technique has allowed us to marry the advantages of REMPI (mass resolution, high collection efficiency) with 90-MHz resolution possible with excitation by continuous laser radiation. This new technique may play a role in a variety of experiments for which high-sensitivity and high resolution are required, including measurement of the electron's electric dipole moment.

Chapter 5

Summary and conclusion

At the onset of my Ph.d research, the PbF e-EDM experiment was only an idea. The laboratory had no expertise in making heavy radicals, nor any direct experience with high resolution spectroscopy. The data and methods achieved by myself, Chris McRaven, and Professor Neil Shafer-Ray and presented in this thesis have taken us from this humble beginning to the threshold of an e-EDM measurement. Specifically we have achieved the following:

- The creation of a stable molecular beam source of PbF based on the reaction of Pb and MgF_2.
- The demonstration of resonant enhanced multiphoton ionization (REMPI)detection of the the molecule.
- Experimental measurement and analysis of the rotational spectra of the 0-0 band of the B-X transition of PbF. This measurement determines the rotational temperature of our source.
- Measurement of appearance ionization from the B and D states of the PbF molecule.

This measurement improves the known ionization potential of PbF from 7.5 ± 0.3 eV to 7.54 ± 0.01 eV.

- Achievement of a multiphoton ionization probe of PbF that is doubly resonant with the X-A and A-D transitions. This scheme allows for fully state resolved spectra of the molecule. (5) Direct measurement of the lifetime of the PbF molecule.

- Measurement of hyperfine constants that model the interaction of the unpaired electron in $^{208}Pb^{19}F$ with the ^{19}F nucleus.

- Demonstration of a new type of ultra-sensitive REMPI is reported. Whereas conventional REMPI is typically carried out with pulsed laser systems, this new technique, dubbed pc-REMPI, occurs with a combination of continuous and pseudo-continuous lasers. This technique improves the detection sensitivity of the original PbF REMPI probe by a factor of 100. At the same time, the technique improves the spectra linewidth from 2 GHz to 90 MHz, allowing for full resolution of the hyperfine structure of the molecule.

These accomplishments are a significant step forward toward the realization of an PbF - based measurement of the e-EDM.

Appendix A

A.1 Flux of Effusive Molecular Beam Source

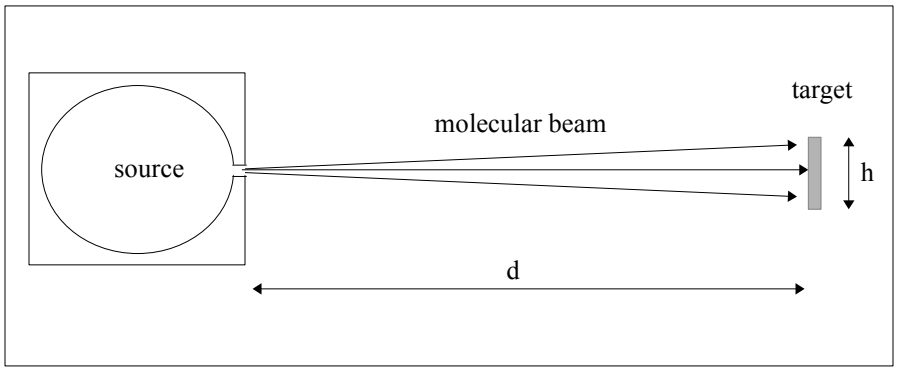

Figure A.1: Schematic diagram of effusive source .

We consider a source of gas on a cell at temperature T_s with a small orifice of area A_s. The rate of escape of particles per differential velocity v_x, v_y and v_z from source can be expressed as,

$$\Gamma(v_x, v_y, v_z) = \frac{1}{2}\rho_s v_z A_s P(v_x, v_y, v_z) \tag{A.1}$$

Here, ρ_s is density of particles in the source, v_z is velocity in source-detection direction, and

$P(v_x, v_y, v_z)$ is the differential probability of finding particle with the velocity v_x, v_y and v_z. This probability is expressed as

$$P(v_x, v_y, v_z) = (\frac{m}{2\pi k T_s})^{3/2} \exp[-mv^2/2k_B T_s]. \tag{A.2}$$

Here, m is mass of the particle and k_B is the Boltzmann constant. To find the rate per differential velocity v_z that particles strike a detector far away, we integrate $\Gamma(v_x, v_y, v_z)$ over the narrow range of v_x and v_y velocity that results in particles that reach the target.

$$\Gamma(v_z) = \int_{-v_{xo}}^{v_{xo}} \int_{-v_{yo}}^{v_{yo}} \Gamma(v_x, v_y, v_z) dv_x dv_y \tag{A.3}$$

We now assume an extent $A_t = \Delta X\ \Delta Y$ of the detection volume that is small enough for $v_{xo} = \frac{\Delta X v_z}{R} \ll \sqrt{\frac{k_B T}{m}}$ and $v_{yo} = \frac{\Delta Y v_z}{R} \ll \sqrt{\frac{k_B T}{m}}$ to be valid. For this case, the integral reduces to

$$\Gamma(v_z) = (\frac{A_t}{4\pi R^2})[\rho_s \sqrt{\frac{1}{2\pi}} (\frac{m}{kT})^{3/2} v_z^3 \exp[-mv^2/2kT]] \tag{A.4}$$

We recognize $\frac{A_t}{4\pi R^2}$ as the strradian extent of the detector. This lead us to write:

$$\frac{d\Gamma(v_z)}{d\Omega} = A_s \rho_s \sqrt{\frac{1}{2\pi}} (\frac{m}{kT})^{3/2} v_z^3 \exp[-mv^2/2kT] \tag{A.5}$$

The total flux can be obtained by integrating over v_z :

$$\Phi = \frac{d\Gamma}{d\Omega} = \frac{1}{2} \bar{v} A_s \rho_s \tag{A.6}$$

Here $\bar{v} = \sqrt{\frac{8k_B T}{\pi m}}$ is an average velocity of the particles at temperature T.

We also can expressed rate of particle reaching the target in the range of velocity dv_z as:

$$\Gamma(v_z) = \rho_t v_z P(v_z) \tag{A.7}$$

Here, $P(v_z)$ is the probability of finding particle with a beam speed v_z. The function $P(v_z)$ is expressed by determined by comparing to Eq A.4 to Eq A.7:

$$P(v_z) = \sqrt{\frac{2}{\pi}}(\frac{m}{kT})^{3/2} v_z^2 \exp[-mv_z^2/2kT]. \tag{A.8}$$

The rate of particle reaching target is obtained by integration over beam speed.

$$\frac{d\Gamma}{d\Omega} = \int \frac{d\Gamma(v_z)}{d\Omega} dv_z \tag{A.9}$$

$$= 4\pi R^2 \sqrt{\frac{8kT}{\pi m}} \rho_t \tag{A.10}$$

Bibliography

[1] *NIST Chemistry WebBook*. NIST Standard Reference Database Number 69. National Institute of Standards and Technology, Gaithersburg MD, 20899 (http://webbook.nist.gov)., 2005.

[2] Ahmed H. Zewail. *J. Phys. Chem*, 100:12701, 1990.

[3] Allan C. G. Mitchell and Mark W. Zemansky. *Resonance Radiation and Excited Atoms*. Cambridge University Press, London, 1971.

[4] Barrow R. F, Butler D, Johns J. W. C, and Powell J. L. *Proc. Phys. Soc*, 73:317, 1959.

[5] Brewer L, James C G, Brewer G R, Stafford F E, Berg R A, and Rosenblatt G M. *Rev.Sci.Instrum*, 33:1450, 1962.

[6] Brown J. M, Colbourn E. A, Watson J. K. G, and Wayne F. D. *J. Mol. Spectrosc*, 55:500, 1975.

[7] C. P. McRaven, P. Sivakumar, and N. E. Shafer-Ray. *Phys. Rev. A*, 75(2):024502, 2007.

[8] C. P. McRaven, P. Sivakumar, and N. E. Shafer-Ray. *Phys. Rev. A*, 78:054502, 2008.

[9] C. S. Wu, E. Ambler, R. W. Hayward, D. D. Hoppes, and R. P. Hudson. *Phys. Rev*, 105:1413, 1957.

[10] C. W. Forsberg, E. C. Beahm, and J. C. Rudolph. *Direct Conversion of Halogen-Containing Wastes to Borosolicate Glass.* Materials Research Society, 1996.

[11] C.B. Collins, B.W. Johnson, M.Y. Mirza, D.Popescu, and I. Popescu. *Phys.Rev. A*, 10:813, 1974.

[12] D. Kawall, F. Bay, S. Bickman, Y. Jing, and D. Demille. *Phys. Rev. Lett*, 92:133007, 2004.

[13] D. L. Feldman, R. K. Lengel, and R. N. Zare. *Chem. Phys. Lett*, 52:413, 1977.

[14] Dickson C and Zare R. N. *Optica Pura Y Aplicada*, 10:157, 1977.

[15] Duschinsky. F. *Z. f. Phys*, 78:586, 1932.

[16] E.M. Purcell and N. F. Ramsey. *Phys. Rev.*, 78:807, 1950.

[17] Eugene. D. Commins, Stephen B. Ross, David DeMille, and Regan B. C. I. *Phys. Rev. A*, 50:2960, 1994.

[18] F. Hoogeveen. *Nucl. Phys*, B341:322, 1990.

[19] F. Hoogeveen. *Nucl. Phys*, B341(322), 1990.

[20] Feldman D. L, Lengel R. K, and Zare R. N. *Chem. Phys. Lett*, 52:413, 1977.

[21] Foster E. W. *University of Lanodon Observatory*, page 469.

[22] Frank Morgan. *Phy. Rev*, 49:47, 1936.

[23] Gamini Dharmasena, Kyle Copeland, Joel H. Young, Rosemary A. Lasell, Timothy R. Phillips, Gregory A. Parker, and Mark Keil. *J. Phys. Chem. A*, 101:6429, 1997.

[24] Gerhard Herzberg F.R.S. *Molecular Spectra and Molecular Structure*. D. Van Nostrand Company (Canada) LTD., 1953.

[25] Green R. B, Hanko L, and Davis S. J. *Chem. Phys. Lett*, 64(3):461, 1979.

[26] Howell and Rochester G. D. *Univ. Durham Phil. Soc. Proc*, 9:126, 1934.

[27] Hudson. J. J, Sauer. B. E, Tarbutt. M. R, and Hinds. E. A. *Phys. Rev. Lett*, 89:023003, 2002.

[28] Hupfield H. *Z. f. Phys*, 54:484, 1929.

[29] I. Kopp and J. T. Hocgen. *Can. J. Phys*, 45:2581, 1967.

[30] J. H. Christenson, J. W. Cronin, and R. Turlar. *Phys. Rev. Lett.*, 13:138, 1964.

[31] J. T. Hougen. *J. Chem. Phys*, 36:519, 1962.

[32] Jenkins F. A and Rochester G. R. *Phys. Rev*, 1937.

[33] Jing Chen and Paul J. Dagdigan. *J. Chem. Phys*, 96:1030, 1992.

[34] K. Balasubramanian. *J. Chem. Phys*, 83:2311, 1985.

[35] K. Kawaguchi, S. Saito, and E. Hirota. *Mol. Phys.*, 55:341, 1985.

[36] K. Ziebarth, R. Breidohr, O. Shestakov, and E. H. Fink. *Chem. Phys. Lett*, 190:271, 1998.

[37] K. Zmbov, J. W. Hastie, and J. L. Margrave. *Trans. Faraday. Soc*, 64:861, 1968.

[38] Knight. A.E. W and Selinger. B. K. *Aust.J.Chem*, 26:1, 1973.

[39] Kozlov M. G and Labzowsky L. N. *J. Phys. B: At. Mol. Opt. Phys*, 28:1933, 1995.

[40] L. E. Brus and J. R. McDonald. *J. Chem. Phys*, 61:97, 1974.

[41] L. I. Schiff. *Phys. Rev*, 132:2194, 1963.

[42] L. Landau. *Nucl. Phys*, 3:127, 1957.

[43] Leo Brewer, C.Geoffrey James, Richard G.Brewer, Fred E. Stafford, Robert A. Berg, and Gerd M. Rosenblatt. *Rev. Sci. Instrum*, 33(12):1450, 1962.

[44] Lumley D. J. W. and Barrow R. F. *J. Phys. B: Atom. Molec. Phys*, 10(8):1573, 1977.

[45] M. Kozlov, Eksp. Teor, and Teor. Fiz. 89:1933, 1985.

[46] M. Kozlov, V. Fomichev, and A. Titov. 20:4939, 1987.

[47] Milinda Rupasinghe and N.E Shafer-Ray. *Phys. Rev. A*, 78:033427, 2008.

[48] Moore C B. *Ann. Rev. Phys. Chem*, 22:387, 1971.

[49] Murthy S. A, Krause D, Li .jr. Z. L, and Hunter L. R. *Phys. Rev. Let*, 63(9):965, 1989.

[50] Neil E. Shafer-Ray. *Phys. Rev. A*, 73:034102, 2006.

[51] Osberghus O and Ziock K. *Z. Naturf*, 11:762, 1956.

[52] P. G. H. Sandars. *Phys. Lett*, 14:194, 1965.

[53] P. G. H. Sandars. *Phys. Lett.*, 14(71):194, 1967.

[54] P. M. Johnson, M. R. Berman, and D. Zakheim. *J. Chem. Phys*, 62:2500, 1975.

[55] P. Sandars. *Atomic. Phys*, 14:71, 1975.

[56] P. Sandars and E. Lipworth. *Phys. Rev.Let*, 13:718, 1964.

[57] P. Sivakumar, C. P. McRaven, and N. E. Shafer-Ray. *Phy. Rev. A*, 77(062508):1, 2008.

[58] P. Sivakumar, C. P. McRaven, P. M. Rupasinghe, T. Zh. Yang, and N. E. Shafer-Ray. Accepted. *Mol. Phys*, 2009.

[59] R. A. Frosch and H. M. Foley. *Phys. Rev*, 88:1337, 1952.

[60] R. Arnowitt, B. Dutta, and Y. Santoso. *Phys. Rev. D*, 64:113010, 2001.

[61] Rick Trebino. *Frequency-Resolved Optical Gating: The measurements of Ultrashort Laser Pulses*. Kluwer Academic, Massachusetts, 2000.

[62] Robert. E. Imhof and Frank. H. Read. *Rep. Prog. Phys*, 40(1), 1977.

[63] Rochester G. D. *Proc. Roy. Soy. A*, 153:407, 1936.

[64] Rochester G. D. *R. Soc. London, Ser A*, 167:567, 1938.

[65] S. E Schewartz and H. S Johnston. *J. Chem. Phys.*, 51:1286, 1969.

[66] Shestakov O, Pravilov A. M, Demes H, and Fink E. H. *Chem. Phys*, 165:415, 1992.

[67] Singh O. N, Srivastava M .P, and Singh I. S. *Can. J. Phys*, 47:1639, 1969.

[68] Spears K. J and Rice S. A. *J.Chem.Phys*, 55:5561, 1971.

[69] T. D. Lee and C. N. Yang. *Phys. Rev*, 104:254, 1956.

[70] W. C. Wiley and I. H McLaren. *Rev. Sci. Instr*, 26, 1955.

[71] Wien. W. *Ann. d. Phys*, 73:483, 1924.

[72] Z. W. Liu and H. P. Kelly. *Phys. Rev. A*, 45:R4210, 1992.

[73] Ziebarth K, Setzer K. D, Shestakov O, and Fink E. H. *J. Mol. Spec*, 191:108, 1998.